Wissenschaftliche Arbeit zur Erlangung des akademischen Grades Master of Science (M.Sc.)

Studies on an in-situ calibration method for the IceCube multi-PMT optical module using radioactive decays

im Fachgebiet Physik

Autorin:	Tabea Maria Eder
Matrikelnummer:	409190
E-Mail Adresse:	t_eder04@wwu.de
Erstgutachten:	Prof. Dr. Alexander Kappes
Zweitgutachten:	Dr. Volker Hannen

2019

Inhaltsverzeichnis

Declaration of Academic Integrity

I hereby confirm that this thesis on "Studies on an in-situ calibration method for the IceCube multi-PMT optical module using radioactive decays" is solely my own work and that I have used no sources or aids other than the ones stated. All passages in my thesis for which other sources, including electronic media, have been used, be it direct quotes or content references, have been acknowledged as such and the sources cited.

Münster, 04 January 2019 _____

I agree to have my thesis checked in order to rule out potential similarities with other works and to have my thesis stored in a database for this purpose.

Münster, 04 January 2019 _____

1. Introduction

Neutrino astronomy is promising to give an insight into the production and acceleration of the most energetic particles we know of, the ultra-high energy cosmic rays. High energetic cosmic neutrinos are very useful cosmic messengers since they offer accurate information about their origin and thus can be used to determine the acceleration processes of cosmic rays. The largest neutrino observatory existing up to now is the IceCube Neutrino Observatory at the South Pole with one cubic kilometer of instrumented glacial ice. It is a detector making use of Cherenkov light produced by charged particles emerging from interactions of the neutrinos with the ice. The light is detected by 5160 optical sensors called photomultiplier tubes, each deposited in one optical module [1]. No point source of high energetic cosmic neutrinos was found until now, but an extension of IceCube called IceCube-Gen2 is the planing phase. Its larger detector volume shall increase the statistics and lead to the discovery of a point source, if there is one to be discovered [2].

A first step of an IceCube extension is the IceCube Upgrade planed to finish constructions in 2023. New, improved optical modules will be deployed, one of them being the multi-PMT Digital Optical Module (mDOM) [3]. In comparison to the hitherto used modules it contains several PMTs. This results in several advantages but also new challenges as the now necessary calibration of the PMTs in one module. The calibration is required for correcting for different sensitivities and timing of the PMTs [4]. This has to be done to achieve accurate knowledge on the energy and direction of the neutrinos used to learn about the origin and acceleration mechanism of high energetic cosmic rays.

The more accurate the knowledge about the energy and direction of the neutrinos is, the more there can be learned and drawn from detected neutrinos. The PMTs deliver information about the number and timing of detected photons. These two informations are used to get the energy and direction of the neutrinos [5]. Photon numbers and timing should therefore be known well and it has to be known how efficient the PMTs detect photons and what their absolute timing is in order to correct for differences between the PMTs.

This thesis investigates the applicability and accuracy of a method for the time calibration of the PMTs in one mDOM. This method is already used for the calibration of a similar optical module in a different Cherenkov neutrino detector [6]. The calibration method for the mDOM makes use of optical background produced in the glass pressure vessel surrounding the module. This background is produced by radioactive decays leading to the emission of Cherenkov light and scintillation light in the vessel glass. Coincident hits caused by the Cherenkov light are the basis of the calibration algorithm.

Section 2 gives an overview of the motivation behind the IceCube Neutrino Observatory, its setup, planed extensions and the new optical modules called mDOM. The calibration method investigated in this thesis is introduced in Section 3. The Geant4 simulation

used to study the calibration method is introduced in Section 4 and the simulation studies are described in Section 5. Finally the application of the calibration method to an experimental test setup is described in Section 6 followed by the summary and outlook in Section 7.

2. The IceCube Neutrino Telescope

In the era of multi-messenger astronomy high energetic neutrinos are, besides cosmic rays, photons and gravitational waves, an important piece of the puzzle of extraterrestrial particle sources. On the way of solving it, methods were invented to detect these rarely interacting particles. The IceCube Neutrino Observatory, as well as e.g. the KM3NeT [7] neutrino telescope, uses the Cherenkov effect as detection mechanism.

This chapter starts with a brief introduction to cosmic rays and neutrino astronomy to provide the main motivation for the construction of neutrino telescopes. It then continues with the detection principle, the layout of the IceCube detector and its future upgrades. The last section deals with a new optical module called multi-PMT Digital Optical Module (mDOM).

2.1. Cosmic Rays and Neutrino Astronomy

Not all particles with extraterrestrial origin arriving at the earth are actually called cosmic rays. This label is reserved for stable, charged particles of cosmic origin [8]. About 90% of them are protons [9], the rest is made up of nuclei of helium ($\sim$ 9% [9]) and heavier elements, as well as electrons, positrons and anti-protons [8]. These particles can have huge energies up to at least 10^{20} eV (see Fig. 1), several orders of magnitude higher than energies achieved by human-made accelerators. A very interesting, yet unanswered question is how cosmic rays achieve these high energies. Some of these particles, the primaries, are directly accelerated by cosmic particle sources whereas others are produced by the primary particles interacting with interstellar gas [8]. The accelerating sources are not identified by now, but there are some candidates for both galactic and extragalactic sources. Possible galactic accelerators are mainly supernova remnants, but also pulsars and binary star systems including a black hole or a neutron star [10]. The measured energy spectrum of cosmic rays shown in Fig. 1 shows several prominent features, as e.g. the "knee" at $\sim 10^{15}$ to 10^{16} eV. Possible explanations of this steepening include that particles with energies below the "knee" originate from galactic sources, which are then partly running out of power. The "ankle" at $\sim 10^{18.5}$ eV could reflect the beginning dominance of extragalactic sources over galactic sources [8]. Extragalactic accelerators could be active galactic nuclei, gamma ray bursts and starburst galaxies [10]. It is not yet known what the acceleration processes are at these high energies, but a prominent theory is the first order Fermi acceleration. It describes the acceleration of charged particles by shock fronts propagating through magnetized plasma [9] [11]. Cosmic rays themselves can be confined to the acceleration region or be deflected by magnetic fields, losing their directional information [10]. However, one way to find out about accelerating sources and mechanisms is via neutrino astronomy.

Neutrinos are leptons with no electric charge interacting via gravitation and weak interaction. There are three weak eigenstates $|\nu_l\rangle$ with the lepton flavours $l = e, \mu, \tau$ and three mass eigenstates $|\nu_i\rangle$. The mass and flavour eigenstates can not be directly

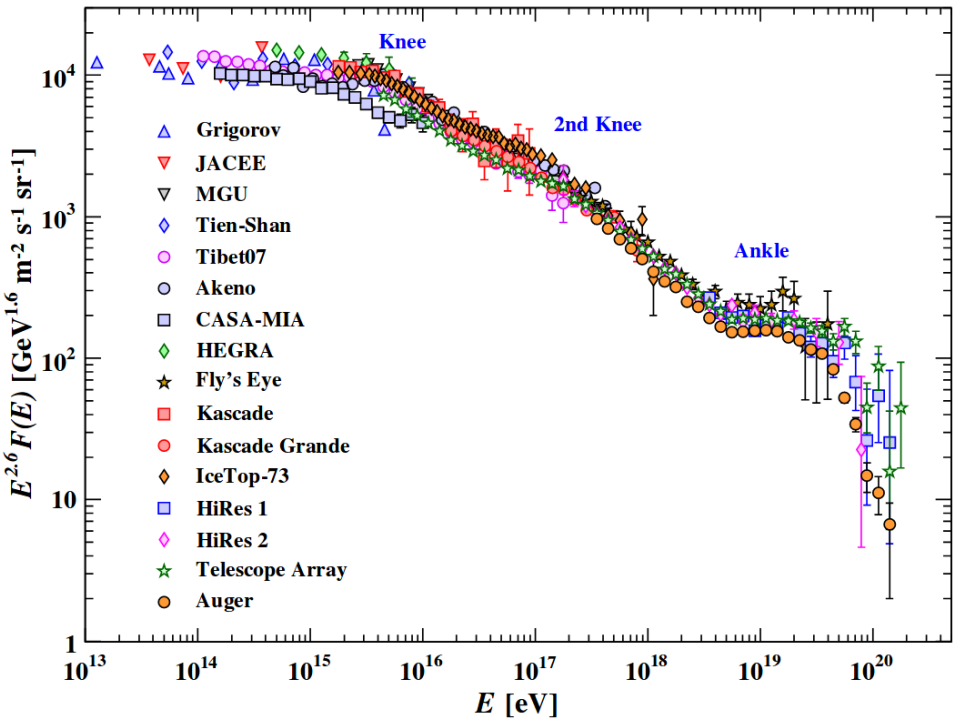

Figure 1: Upper part of the measured energy spectrum of cosmic rays including all particles, where E is the energy-per-nucleus and F is the flux. The flux has been multiplied by $E^{2.6}$ to show some features of the spectrum better. The legend indicates the experiment which measured the data point. Plot taken from [8].

associated with each other, but they are related by the neutrino mixing matrix. This gives rise to neutrino oscillation describing the phenomenon that a neutrino created in a certain flavour eigenstate will take part in subsequent weak interactions in any of the three flavour eigenstates with a certain probability. The masses of the neutrinos are very small and only upper bounds exist for them up to now (2018). The sum of the neutrino masses[1] for example is confined to below 0.2 eV [8]. Since neutrinos only interact via gravitation and weak interaction, the cross section for a neutrino interaction is very small[2]. Neutrinos that are produced far away, for example in other galaxies, are very likely to get to earth without changing direction or losing energy, except if they come across very dense environments like a black hole. Their rare interaction makes them an ideal messenger for information about their origin.

If a source accelerated protons or heavier nuclei they would produce neutrinos either by interaction with radiation or matter. The energy spectrum of these neutrinos is expected to start in the low GeV range. Photons could also be produced during these

[1] The sum of neutrino masses is defined as $m_{\mathrm{tot}} = \sum_\nu (g_\nu/2) m_\nu$ where g_ν is the number of spin degrees of freedom for neutrino and anti-neutrino. It is 4 for Dirac neutrinos and 2 for Majorana neutrinos.

[2] See [12] for neutrino cross sections on different energy scales.

hadronic acceleration processes and additionally by accelerated electrons, although not at the same energy scales. Photons in the PeV energy region would be expected to be of hadronic origin. However, they get absorbed by pair production with photons from the cosmic microwave background and cannot travel further than the size of our galaxy [10].

2.2. Detection Principle

The small interaction cross section of neutrinos makes them advantageous cosmic messengers on the one hand but hard to detect on the other hand. Thus a proper detection principle is necessary. Since the interaction probability increases with a larger target volume, the IceCube neutrino detector uses one cubic kilometre of ice as detection medium. Neutrino interactions within the ice can produce charged particles which again produce Cherenkov light if they overcome a certain energy threshold. This light is then detected by optical sensors called photomultiplier tubes (PMTs), whose working mechanism is explained in Section 2.3.

2.2.1. Cherenkov Effect

The Cherenkov light was experimentally first discovered and analyzed by P.A. Cherenkov in the 1930s [13]. The theoretical explanation of the phenomenon was developed by I.M. Frank and I.E. Tamm [14]. Cherenkov light is produced by charged particles moving through a medium with a velocity v faster than the phase velocity of light c_n in the particular medium. This implies

$$v > \frac{c}{n} = c_n \tag{1}$$

or in terms of the kinetic energy E_{kin} of the particle

$$E_{\text{kin}} > mc^2 \left(\frac{n}{\sqrt{n^2 - 1}} - 1 \right), \tag{2}$$

where c is the speed of light in vacuum, n the refractive index of the medium and m the mass of the charged particle.

A charge moving through a medium polarises it temporarily along its path. The emerging dipoles emit electromagnetic waves which interfere destructively in the far field if $v < c_n$. For $v > c_n$ the interference is constructive along a cone with opening angle θ around the direction of the charged particle. In other words: photons are emitted under an angle θ to the direction of the charged particle. The angle obeys

$$\cos\theta = \frac{1}{\beta n}, \tag{3}$$

where $\beta = v/c$. The case of constructive interference is illustrated in Fig. 2. The distance traveled by the charged particle in a time t is given by vt, whereas the emitted electromagnetic waves propagate by $c_n \cdot t < vt$ [13].

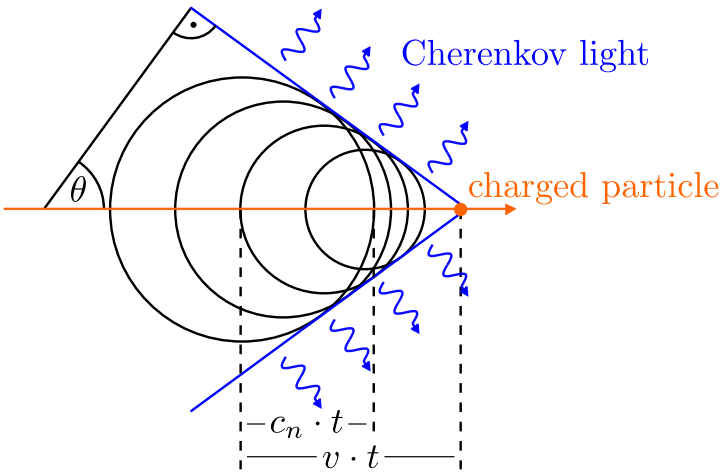

Figure 2: Scheme of the emergence of Cherenkov light. Inspired by [15].

The number of emitted photons with wavelengths between λ_1 and λ_2 by an electron on a path of the length l is given by

$$N_\gamma = 2\pi\alpha \left(\frac{l}{\lambda_2} - \frac{l}{\lambda_1}\right)\left(1 - \frac{1}{\beta^2 n^2}\right), \tag{4}$$

where α is the fine structure constant [14].

The number of emitted Cherenkov photons and the direction of the light provide information about the energy and direction of the charged particle. This is essential for Cherenkov neutrino telescopes, since the charged particles produced by neutrino interactions preserve parts of the neutrinos energy and directional information.

2.2.2. Neutrino Interactions and their Signatures

In the energy region above $\sim 10\,\mathrm{GeV}$ relevant for cosmic neutrinos the dominant interaction for neutrinos with matter is deep-inelastic scattering on a nucleon [10] [12]. This can happen via charged current (CC)

$$\overset{(-)}{\nu}_l + N \rightarrow l^{\mp} + X \tag{5}$$

or neutral current (NC)

$$\overset{(-)}{\nu}_l + N \rightarrow \overset{(-)}{\nu}_l + X. \tag{6}$$

Here l stands for either electron (e), muon (μ) or tauon (τ) and $\overset{(-)}{\nu}_l$ for the corresponding (anti-)neutrino. N is a nucleon and X an hadronic system. Depending on the neutrino flavour and the type of interaction different signatures occur in the detector. The CC interaction of a muon (anti-)neutrino is special in a sense that its signature is a so called muon track (see Fig. 3(a)), which allows for the best angular resolution. The muon takes away most of the energy of the neutrino and produces Cherenkov light along its path

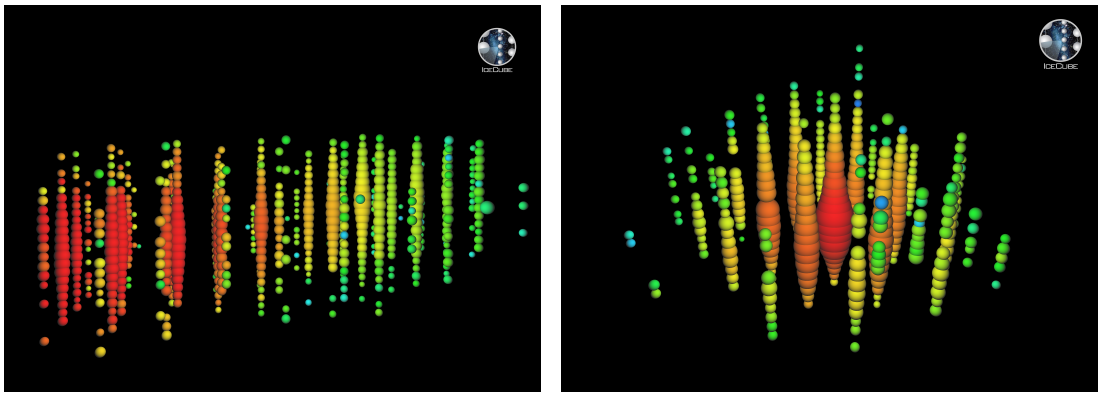

Figure 3: Signature in IceCube of a muon track (left) and a cascade (right). Each bubble stands for one optical sensor. The size of the bubble indicates the amount of detected photons and the color the arrival time, where red is early and blue is late. Courtesy of the IceCube Collaboration.

creating a track like signature in the detector. Most other neutrino interactions have cascade signatures produced by electromagnetic or hadronic cascades (see Fig. 3(b)). These signatures feature worse angular resolution due to their spherical structure [10]. One exception is the CC interaction producing a tauon, which can lead to several signatures because of the tauons short lifetime. For example a double bang event occurs if both the neutrino interaction and the decay of the tauon is contained in the detector volume. This event has comparable angular resolution to the muon track. Other signatures are possible, depending on the decay channel of the tauon and which one of the vertices, neutrino interaction and tauon decay, is contained in the detector [16].

2.3. Photomultiplier Tubes

Photomultiplier Tubes (PMTs) are the actual sensors of IceCube, detecting the Cherenkov light. A PMT is a light detector sensitive to even single photons and typically reaching a time resolution of nano- to hundreds of picoseconds [17]. This chapter explains the basic operation principle and PMT parameters. For further reading see e.g. [18].

A PMT consists basically of a photosensitive area and an electron-multiplying structure (see Fig. 4) consisting of multiple electrodes (dynodes). Photons hitting the sensitive photocathode at the inside of the entrance window can each release one electron through the photoelectric effect into the vacuum inside the PMT. The electrons produced this way are called photoelectrons (pe). A voltage gradient is applied from the photocathode over the dynodes to the anode by a voltage divider circuit. Some PMTs contain a focusing electrode between cathode and first dynode [18] to focus the electrons emitted from the photocathode onto the first dynode. Here the impact of each electron leads, with a certain probability, to emission of secondary electrons. These are accelerated to the next dynode where again secondary electron emission takes place. This multiplication

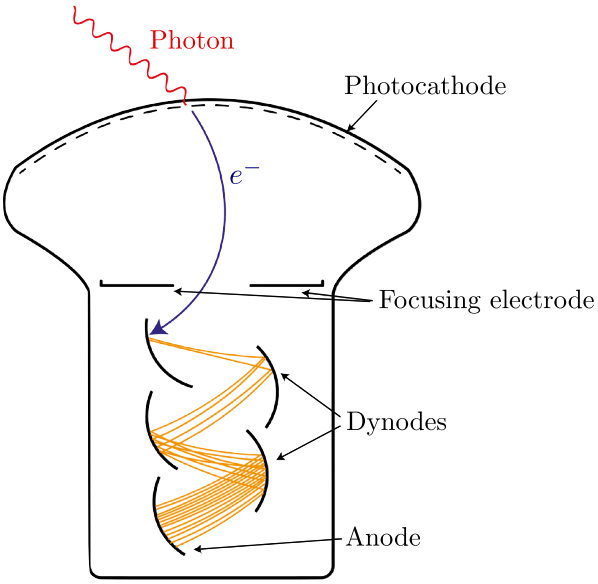

Figure 4: Schematic structure of a PMT. Taken from [19], modified.

process repeats itself at each dynode stage until in the end a measurable current reaches the anode [17].

Each PMT can be characterized by certain quantities, which are important criteria for choosing a suitable PMT for an application and interpreting the measured data. Here, quantum efficiency, gain, time characteristics and dark rate of a PMT are introduced. Some of these parameters depend on the mode chosen for signal processing. The signal can either be given as current or converted to voltage, corresponding to current or pulse mode, respectively [18]. The pulse mode is better suited for detection of single photons and will be used in the measurements of this thesis. Detected photons are in this mode visible in the signal as transient pulses.

Quantum Efficiency Photocathodes are made of semiconductors exhibiting the external photoelectric effect, where the electron is emitted into the vacuum. The probability for an incoming photon to release an electron into the vacuum is described by the quantum efficiency (QE), which is wavelength dependent [17].

Gain The electron multiplication factor of the multiplying structure depends heavily on the geometry and material of the dynodes as well as the applied voltage [17]. It is called the gain and given by the product of collection efficiencies and secondary emission ratios of each dynode. The collection efficiency of the kth dynode is the probability for photoelectrons emitted by it to hit the effective area of the $k+1$th dynode, where secondary electron emission occurs. The secondary emission ratio is the factor by which electrons are multiplied at each dynode [17] [20].

Detection Efficiency The detection efficiency ϵ is defined as the ratio of the number of incident photons on the photocathode to the number of counted photons at the anode. It depends on the operation conditions of the PMT (e.g. applied voltage) and the instrumentation used to process the PMT output signal (e.g. detection threshold level). The detection is amongst others influenced by the quantum efficiency and the collection efficiency of the dynode system [18].

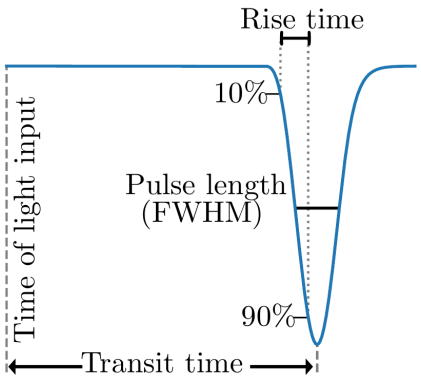

Figure 5: Schematic representation of the time characteristics of a PMT pulse. Taken from [19].

Time Characteristics Another important characteristic quantity of a PMT is its transit time, given by the time a photoelectron needs from the photocathode to the anode (see Fig. 5). The distribution of the transit time can be modelled by a Gaussian whose standard deviation is called the transit time spread (TTS). It decreases with increasing number of photoelectrons per light pulse. The transit time influences the time response of the PMT, whereas the TTS influences the time resolution. A PMT pulse is furthermore characterized by the rise time, defined as the time the pulse needs to increase from 10% of the maximum amplitude to 90%. The fall time is analogously defined on the trailing edge of the pulse. The pulse length can be defined by the full width at half maximum (FWHM) of the pulse [17].

Dark Rate Even if no external light source is present, a PMT will still deliver a signal. The rate of measured pulses of a PMT in complete darkness is called the dark rate if operated in pulse mode. The dark current is the respective current measured with a PMT in current mode in complete darkness [18]. There are multiple origins of dark rate, among them thermionic emission from photocathode and dynodes, leakage current at various points and scintillation from the glass envelope. Dark rate changes significantly with temperature and supply voltage [17].

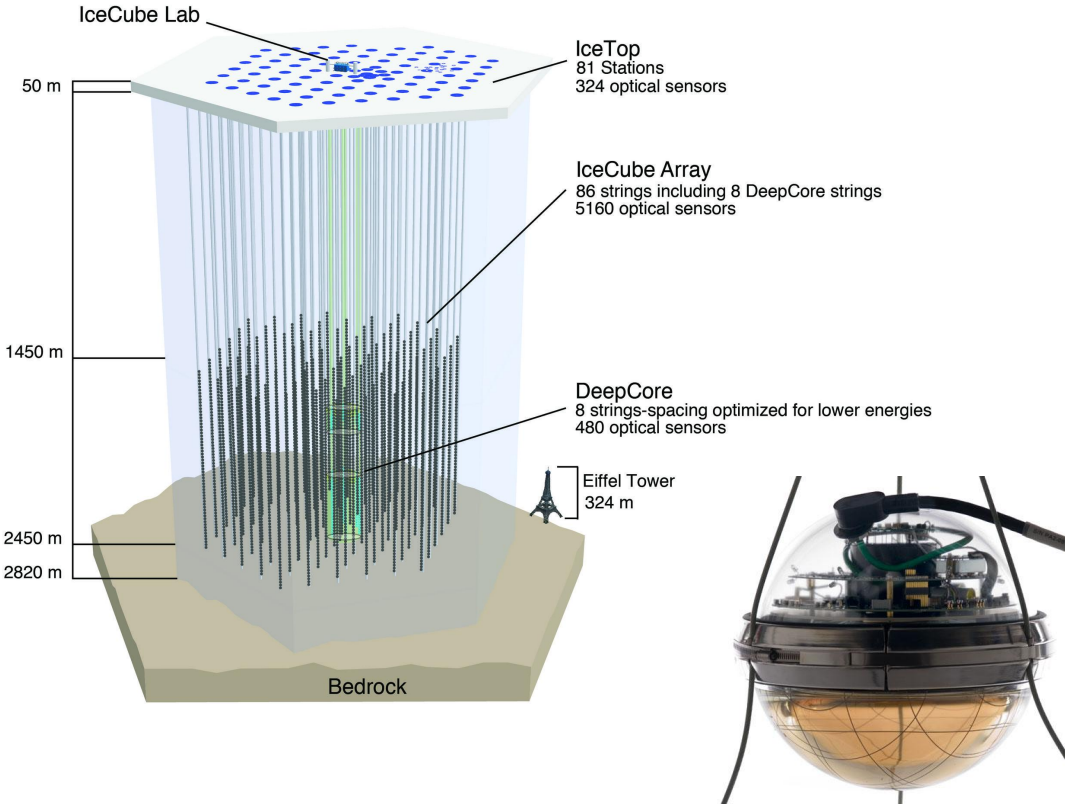

Figure 6: On the left: Detector of the IceCube Neutrino Observatory. Courtesy of the IceCube Collaboration.. On the right: The detector modules used for IceCube, the Digital Optical Module (DOM). Taken from [21].

2.4. The Detector Setup

The IceCube Neutrino Observatory is stationed at the South Pole and uses one cubic kilometer of antarctic ice as Cherenkov medium (see Fig. 6). It is optimized to detect neutrinos with energies from 100 GeV up to PeV [4]. The Cherenkov light is detected by 5160 10-inch photomultiplier tubes facing downwards, each contained in a spherical pressure vessel together with readout electronics constituting a Digital Optical Module (DOM) (right in Fig. 6). The setup of the IceCube detector can be seen on the left side in Fig. 6, where every small black dot stands for one DOM and the vertical lines for the strings to which the DOMs are fixed. 60 DOMs are attached to each vertical string. There are 78 strings with a vertical spacing of 17 m and a horizontal spacing of 125 m, placed between 1450 and 2450 m beneath the surface. For the deployment of the strings, holes were melted into the ice for each of them using a hot water drilling technique. Afterwards the water freezes again, putting the modules in fixed positions and temporary high pressure up to 690 bar on them. The detector includes a denser spaced area with additional eight strings (in green), called DeepCore and optimized for low energies down to 10 GeV. At the surface are additional 324 optical sensors installed for IceTop (in blue), which serves as a surface detector for cosmic rays and veto and

calibration detector for IceCube [1].

2.5. Future IceCube Upgrades

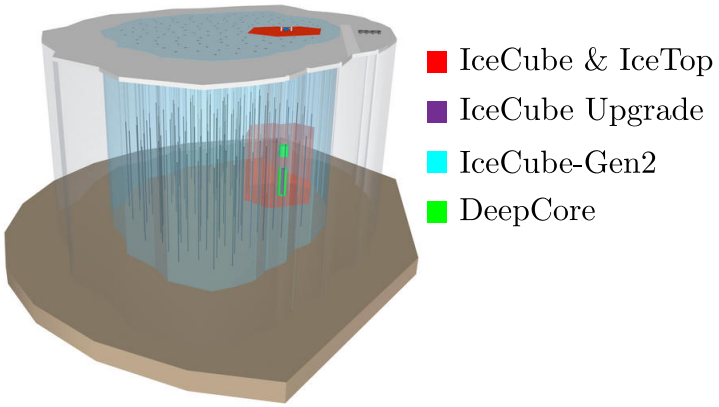

Figure 7: Schematic design for IceCube-Gen2. Courtesy of the IceCube Collaboration, modified.

IceCube-Gen2 is a proposed extension of the IceCube Observatory which expects to discover i.a. point sources of cosmic rays with its increase in sensitivity, angular resolution, detection rates and the observable energy scale. The detection volume shall be increased and new optical modules installed [2]. The IceCube detector will be integrated into the new one, as can be seen in Fig. 7. The red area depicts the IceCube detector with DeepCore in green, the blue area is the IceCube-Gen2 expansion. An extension of the surface array is also planned.

The IceCube Upgrade is an ongoing project which is planned to be completed by 2023. It will contain seven strings in the DeepCore area (purple area in Fig. 7), containing new optical modules. One of the modules is the multi-PMT digital optical module (mDOM) [3].

2.6. The multi-PMT Digital Optical Module (mDOM)

The mDOM is a new digital optical module which is planned to be deployed in the antarctic ice, as already mentioned. The optical module used for the current IceCube detector (right in Fig. 6) consists of a single 10-inch PMT inside a pressure vessel made of glass, including also the readout electronics. The mDOM (left in Fig. 8) contains 24 3-inch PMTs instead of one big PMT, which results in several advantages. These include an increased photocathode area per module, improved nearly isotropic 4π angular acceptance and intrinsic angular resolution through the segmented sensitive area. In addition it is possible that several photons arriving at once hit multiple PMTs instead of only one, which allows for easier photon counting and enables the detection of more photons for one module without saturation. Another new feature is the possibility of local coincidences between the PMTs of one module. For an extensive discussion of the

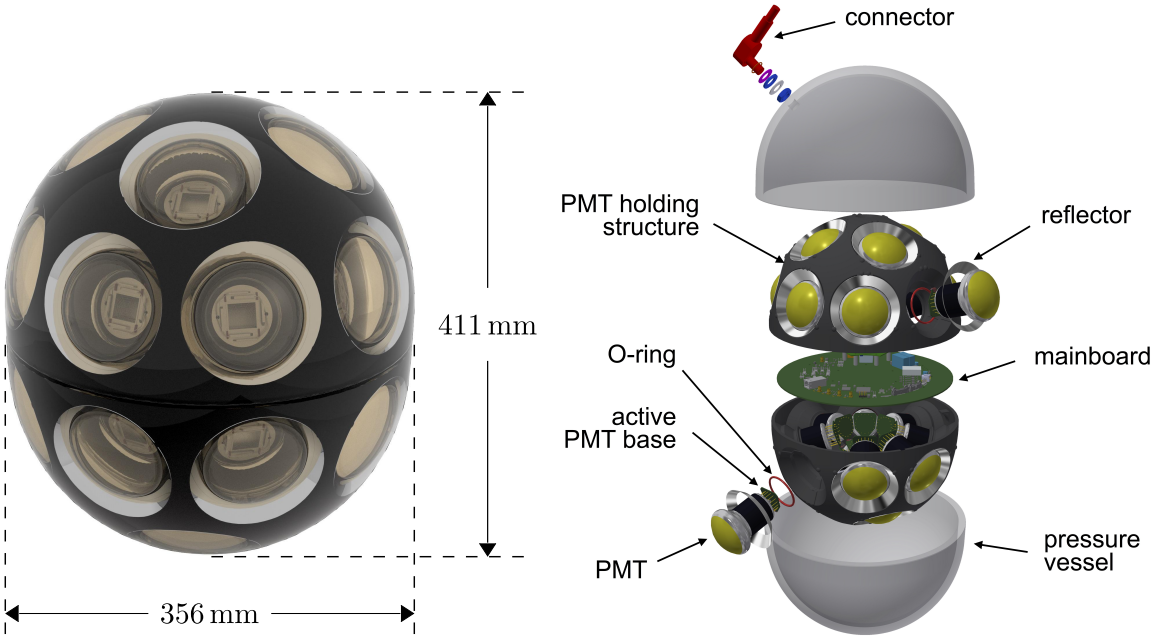

Figure 8: Renderings of the closed and opened mDOM. Courtesy of the IceCube Collaboration.

design of the mDOM and its properties see [4].

The 24 PMTs are each surrounded by reflective cones, further increasing the effective detection area. PMTs and cones are placed in a black, photon absorbing holding structure. The PMT baseline model is the Hamamatsu R12199-02. The bases of the PMTs and the main board are placed inside of this structure, as seen on the right in Fig. 8. The whole construction is surrounded by a 13 mm thick pressure vessel made of borosilicate glass from Vitrovex [22] with outer dimensions of 411 mm diameter at the long and 365 mm at the short axis. The vessel is designed to withstand a pressure of at least 700 bar. The glass is optically coupled to the PMTs by a layer of silicone gel (QGel900 from Quantum Silicones [22]) to reduce refraction at the boundaries. The thickness of the gel layer varies and is about 2 mm at its thinnest. O-rings surrounding the cylindrical parts of the PMTs prevent the gel from getting in contact with the electronics [4].

In contrast to the DOM, the mDOM does not have a spherical shape. Its pressure vessel consists of two half spheres connected by a cylindrical part, which was added to create more space inside the module without increasing the same diameter. This has to be taken into account since the price for drilling increases with the size of the hole and therefore with the size of the module. Each half vessel contains twelve symmetrically arranged PMTs in two rings, one ring at the pole with four PMTs and one at the equator containing eight PMTs. The latter PMTs partly lie in the cylindrical part of the mo-

dule. The asymmetric geometry of the module leads for example to different detection efficiencies between PMTs at the pole and in the middle. From now on it will be spoken of polar and equatorial PMTs and rings.

3. Time Calibration of multi-PMT Optical Modules using Radioactive Decays

As described in Section 2.1 the main goal of the IceCube Neutrino Observatory is to explore the sources of cosmic rays by looking at the origin of cosmic neutrinos. The desired information about the neutrinos are their energy and direction, which are determined by the number of detected photons and their arrival times, respectively [5]. Uncertainties on these quantities will therefore transfer to uncertainties on neutrino energy and direction. There are multiple factors influencing the reconstruction quality, as e.g. the signature type of the neutrino event [5], optical properties of the ice such as the scattering length, noise hits and time jitter of PMTs and other electronics [10].

Apart from these factors, the time and sensitivity calibration of the PMTs give rise to additional uncertainties. The calibration estimates the relative detection efficiency and time differences between the PMTs. Time differences arise due to different transit times and time delays from readout electronics [23]. Efficiency differences occur e.g. because of different quantum efficiencies.

As one mDOM contains multiple PMTs not only a calibration between different modules (inter-mDOM calibration) is required, but also between the PMTs in one module (intra-mDOM calibration). This thesis aims at developing an algorithm for the intra-mDOM calibration, especially the time calibration, using background light produced by radioactive decays in the mDOM pressure vessel.

The calibration has to be able to be done in situ, meaning after the deployment of the modules in the deep ice at South Pole. Another possible calibration method would be using LEDs (light emitting diodes) installed in the mDOM. An advantage of the method using optical background is the independence on any additional electronics. It could be done in a module even if the LEDs were broken.

3.1. Requirements to the Calibration Algorithm

This is a rough estimation of the required accuracy for the time calibration. For this, first the transit time spread of the PMTs is investigated, as it limits the time resolution of a PMT. As mentioned in Section 2.3 the TTS depend on the mean number of photoelectrons per pulse μ. In [24] it has been stated that the maximal requirement to the dynamic range of the optical modules is 30pe/10 ns. In [25] the TTS has been measured in dependency of μ for PMTs of the baseline type for the mDOM. The maximal TTS at low illumination level is at about 1.4 ns. At $\mu = 30$ pe the TTS is at about 0.3 ns. This should be understood as a lower bound, because the requirement of 30pe/10 ns is valid for the whole module and the photons will be distributed among the 24 PMTs.

Another contribution to the time uncertainty is the inter-mDOM calibration. The inter-

DOM calibration in the current IceCube detector will be taken as an estimation of this contribution. The procedure for the calibration is called Reciprocal Active Pulsing Calibration (RAPCal) and is described in [1]. It achieves a time accuracy of 1.2 ns.

The intra-mDOM time calibration should not deliver a significant amount of uncertainty to this. As $\sqrt{0.3^2 + 1.2^2}\,\text{ns} \approx 1.237\,\text{ns}$ an additional uncertainty of 0.40 ns would lead to an increase of 1%, an additional uncertainty of 0.18 ns to an increase of 5%. This estimation is however not very sophisticated, since it includes only two influences on the time uncertainty. For a complete analysis of the requirements on the time uncertainty, the overall time accuracy required to achieve the physical goals of the experiment would have to be investigated and then an analysis of all components contributing to the time uncertainty.

3.2. Calibration Method used in KM3NeT

For the calibration method a mechanism used in KM3NeT is adapted, as suggested in [4]. KM3NeT is a currently build Cherenkov neutrino telescope similar to IceCube using the Mediterranean Sea as detection medium [7]. The detector modules are spherical multi-PMT digital optical modules (KM3NeT DOMs) each containing 31 3-inch PMTs (see Fig. 9). The in situ intra-DOM calibration of a deployed pre-production model (PPM-DOM) and a prototype detection unit (PPM-DU) consisting of a single string with multiple optical modules have been done using Cherenkov light produced by decays of potassium 40 isotopes (^{40}K) naturally occurring in the sea water. For details see the PhD thesis of Jonas Reubelt [23].

^{40}K decays via β^--decay with a branching ratio of 89.28 %

Figure 9: Km3NeT multi-PMT digital optical module containing 31 3-inch PMTs in a spherical pressure vessel. Taken from [26].

$$^{40}\text{K} \rightarrow {}^{40}\text{Ca} + e^- + \bar{\nu}_e \tag{7}$$

where the maximum electron energy is at about 1311 keV. With a branching ratio of 10.66% ^{40}K undergoes electron capture followed by emission of a gamma with an energy of about 1461 keV [27]:

$$^{40}\mathrm{K} + e^- \rightarrow {}^{40}\mathrm{Ar}^* + \nu_e \rightarrow {}^{40}\mathrm{Ar} + \gamma. \tag{8}$$

The gamma can produce an electron by Compton scattering with an energy of about 1.3 MeV at maximum. Electrons produced by these two processes can overcome the Cherenkov threshold in the sea water over a distance of about 1 cm and represent nearly point like photon sources [23].

Together with this Cherenkov light bioluminescence represents the main source for optical background in KM3NeT. Photons from these two background sources are distinguishable when looking at coincidences in the nanosecond range. Coincidences are hits on different PMTs of the same module occurring in a certain time window. A typical size of the time window for coincidences is 20 ns. Coincidences can be classified by their manifold, meaning how many PMTs are hit in the respective time window. Higher manifolds include lower ones, a three-fold coincidence for example can also be seen as three two-fold coincidences. Another distinction can be made between random and genuine coincidences. Random coincidences are dominant at twofold coincidences, whereas genuine ^{40}K coincidences are dominant from three- to sevenfold coincidences. The coincident rate decreases with increasing multiplicity. The calibration method of KM3NeT aims at using genuine ^{40}K twofold coincidences [23].

This is possible by looking at a histogram of the hit time differences of coincident hits for each PMT combination (see Fig. 10). Assuming two PMTs i and j with hit times t_i and t_j, the hit time difference is given by $\Delta t = t_i - t_j$. The distribution can be described by a Gaussian, whose mean corresponds to the relative time offset between the corresponding PMTs. The integral is proportional to the decay rate of ^{40}K and depends on the detection efficiencies of the two PMTs and the angular distance between them. The width is influenced by the TTS of the PMTs, scattering properties of the water and the fact that the ^{40}K isotopes represent no fixed point source but are equally spatially distributed in the water. A vertical offset occurs due to random coincidences [23].

To get the efficiencies differences and time offsets of all PMTs relative to a reference value different algorithms can be used, which are described in [23]. They all use the Δt-distributions of every possible combination of two PMTs in the module. The fit functions of the Δt-distributions are not independent from each other but each share parameters with fit functions of other PMT combinations. One calibration algorithm is the global fit, where the fit functions of all Δt-distributions are optimized at once.

A time accuracy of less than 1 ns could be achieved at a test with the prototype detection unit.

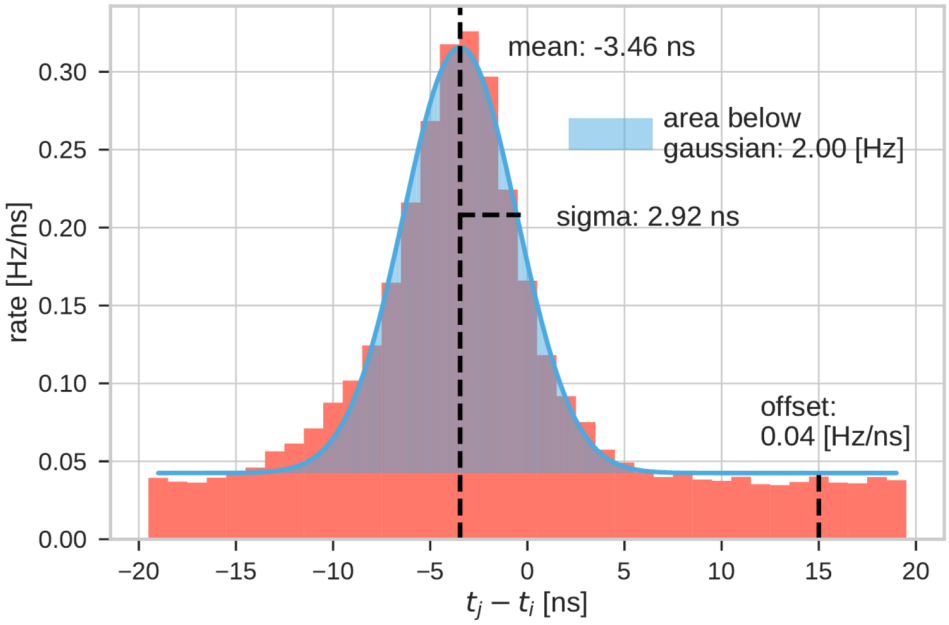

Figure 10: Distribution of hit time differences for a pair of PMTs in a KM3NeT optical module, fitted with a Gaussian. Plot taken from [23].

3.3. Application of the Calibration Method to the mDOM

The introduced calibration algorithm can not be transferred to the mDOM in the glacial ice without adjustments since there are a two major differences.

1. The glacial ice barely exhibits optical background [4]. But the glass of the pressure vessel is also a source of radioactive decays and Cherenkov light. The decays are assumed to be equally distributed in the glass. Which isotopes are found in the vessel glass and which are relevant for the production of Cherenkov light will be discussed in Section 3.4. Scintillation can also be produced by radioactive decays in the glass but on larger time scales than the emission of Cherenkov light [19].

2. The mDOM does not have a spherical pressure vessel in contrast to the KM3NeT DOM. This leads to two different types of PMT: polar and equatorial ones. The latter partly lie in the cylindrical part and thus have slightly different shaped reflective cones. The bottom line is that equatorial PMTs have a slightly higher detection efficiency than polar PMTs, as is shown in Section 5.1.

The application possibility of the described calibration method to the mDOM will be studied in this work. This is first done by simulation studies with a Geant4 [28] simulation of the mDOM (Section 5) and then tested with an experimental setup measuring the Δt-distribution for two PMTs in an mDOM-half vessel (Section 6).

3.4. Measuring Radioactive Decays in the mDOM Glass Vessel

In the scope of this thesis an experimental test setup is build to test the calibration mechanism using Cherenkov light. First of all, the used Vitrovex glass vessel is analysed with gamma spectroscopy to determine the radioactive isotopes in the glass and their activities. In the following the general operation principle of a gamma detector and the gamma spectrum analysis is described.

In an ideal detector for gamma spectroscopy the energy of the gamma rays is linearly transferred to an electric current. The gamma rays interact with the detection medium via photoelectric effect, Compton effect or pair production. The Compton scattering leads to a continuous background, whereas the photoelectric effect converts the full gamma energy into charge and contributes to the so called full energy peak (FEP) in the spectrum. Via these FEPs in a spectrum the isotopes contained in a sample can be identified. One detector type for gamma spectroscopy are semiconductor detectors like the Ge-detector consisting of a reverse biased p-n junction [29].

A short description of the following analysis is given in [30] and [31], an extensive discussion can be read in [29]. The activity A_0 of an isotope with gamma energy E_0 can be calculated as

$$A_0 = \frac{S_0}{t_m \cdot \epsilon \cdot I} \tag{9}$$

where S_0 is the net area of the FEP, t_m the duration of the measurement corrected for dead time, ϵ the full-energy peak efficiency given by the number of counts detected in the FEP area to the number of gamma rays emitted by the sample and I the branching ratio. Notice that in a chain I the relevant branching ratios of all previous isotopes have to be taken in to account too. ϵ is calculated for all relevant energies using a Geant4 simulation from Pawel Mekarski from the University of Alberta. Fig. 11 shows the efficiency spectra calculated from the simulation data. The net S_0 is calculated by

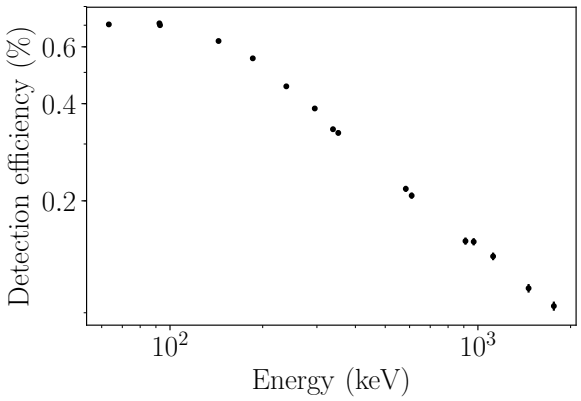

Figure 11: FEP efficiencies calculated with a Geant4 simulation of the measurement setup in double logarithmic scale.

$$S_0 = T_0 - B_0, \tag{10}$$

where T_0 is the total number of counts in the FEP and B_0 the number of background counts contributing to the FEP. These are calculated by fitting the FEP with a Gaussian with linear background to determine the peak region. The background counts are then calculated by

$$B_0 = \frac{n}{2}\left(\frac{B_\mathrm{L}}{m} + \frac{B_\mathrm{U}}{m}\right). \tag{11}$$

The geometrical meaning of this is illustrated in Fig. 12. n is the number of channels in the peak region, m the number of channels additionally used at each side of the peak to estimate the background and B_L and B_U the counts in the channels in the lower and upper background region respectively [29].

The analysis of the gamma spectrum in this thesis is leaned on the analysis in [19]

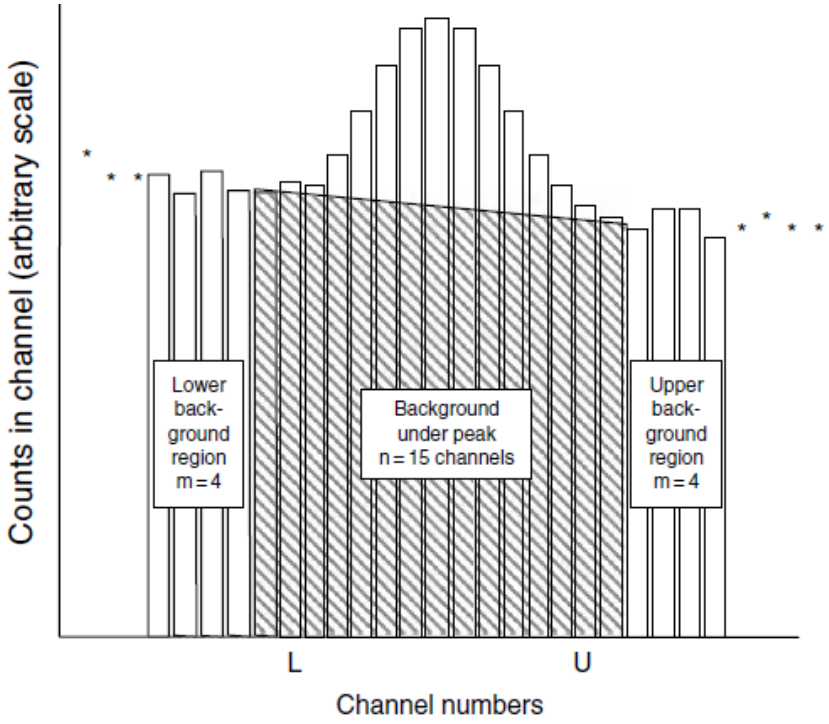

Figure 12: Illustration of the calculation of the background counts at a full energy peak. Taken from [29].

and only the peaks found there are used here for the activity calculation. The three natural decay chains ^{238}U, ^{235}U and ^{232}Th as well as ^{40}K were found in the glass. If undisturbed for long enough, the natural decay chains are in secular equilibrium in a sample [32]. This is assumed to be the case here. From the secular equilibrium follows that all isotopes in a chain are expected to have the same activity. All gamma energies belonging to isotopes from the same decay chain should lead to the same activity. Only those peaks are used for the activity calculation which do not overlap with other peaks.

To calculate the activities of the isotopes in a sample correctly, the background from external sources has to be estimated. The glass vessel is deposited in a lead cube insulating the vessel partly but not completely from external background. To calculate the remaining background two measurements are done, one with the glass vessel inside the lead cube and one background measurement without the vessel. The two spectra after calibration can be seen in Fig. 13. They are slightly shifted with respect to each other, probably because they were not measured with the same setup settings due to an inevitable break and therefore had to be calibrated separately.

The activities per kilogram, called mass-specific activities, for the isotopes also analysed in [19] for the three natural decay chains and ^{40}K can be seen in Table 1. The activities of the isotopes are partly means of activities from several gamma energies. These activities should be the same, since they belong to the same isotope, but they are not for all although always in the same order of magnitude. The isotopes of one decay chain should also have the same activities, which is true for the ^{232}Th-chain but not for the ^{235}U-chain. This could be because the glass is not completely in secular equilibrium. But this would not explain the differences in the activities of same isotopes, so the either the uncertainties may not be estimated correctly or there is a mistake in the analysis. Another disagreement is there between the specific activities of this thesis and the ones measured in [19]. There, three small Vitrovex glass samples (no half vessels) from the same production batch as the half vessel measured in this thesis are analysed, but the activities from the vessel are roughly smaller by a factor of two. This could hint at a systematic mistake somewhere in the analysis made in this thesis, which influences the activities of all energies in the same way. In order to avoid the risk of such mistakes, the analysis of gamma spectra should be done by an automated method if further glass samples will be analysed. This would save time and differences in activities could be traced back to differences in the glass and not the analysis.

In this measurement, the small glass samples measured in [19] and a small Vitrovex glass sample measured at the University of Alberta (see also [19]), ^{40}K dominates with about one order of magnitude over the natural decay chains. But in [19] also a Vitrovex vessel from a production batch in the early 2000s was measured with no measurable amount of ^{40}K, indicating that the amount of ^{40}K depends strongly on the production batch. However for this thesis it is assumed that ^{40}K is dominant in activity and therefore the most important producer of Cherenkov light.

Table 1: Mass-specific activities for the Vitrovex half vessel from the gamma spectroscopy measurement done in the scope of this thesis and for the three samples from [19].

Isotope/Decay chain	Mass-specific activity (Bq/kg))			
	Half vessel	Sample 1	Sample 2	Sample 3
^{214}Bi	2.10 ± 0.07	4.01 ± 0.16	4.29 ± 0.17	4.24 ± 0.14
^{214}Pb	2.35 ± 0.04	4.82 ± 0.12	4.83 ± 0.14	5.19 ± 0.15
^{234}Th	1.83 ± 0.28	5.2 ± 0.9	4.8 ± 1.2	4.49 ± 3.3
^{238}U-chain	2.09 ± 0.10	4.53 ± 0.10	4.61 ± 0.19	4.69 ± 0.10
^{208}Tl	0.70 ± 0.04	1.38 ± 0.20	1.32 ± 0.21	0.97 ± 0.14
^{212}Pb	0.687 ± 0.025	1.42 ± 0.10	1.34 ± 0.11	1.04 ± 0.20
^{228}Ac	0.68 ± 0.06	1.31 ± 0.21	1.34 ± 0.22	1.42 ± 0.24
^{232}Th-chain	0.690 ± 0.024	1.39 ± 0.09	1.34 ± 0.09	1.07 ± 0.10
^{235}U-chain	0.19 ± 0.04	0.56 ± 0.07	0.61 ± 0.07	0.62 ± 0.16
^{40}K	31.9 ± 0.7	53.6 ± 1.7	57.5 ± 1.8	66.2 ± 1.2

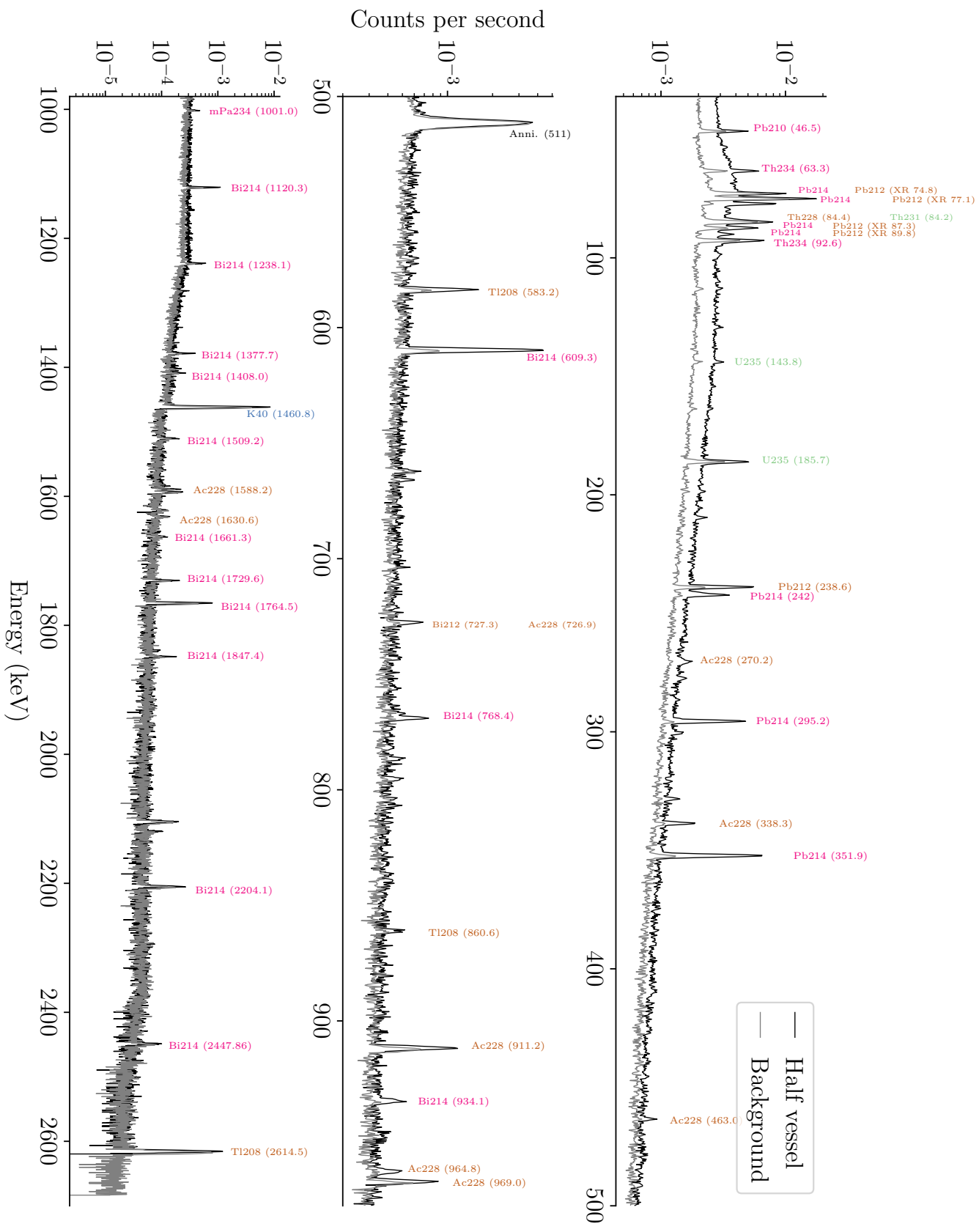

Figure 13: Gamma spectra of glass vessel and background measurement. Different decay chains are marked with different colours.

4. Geant4 Simulation of the mDOM

The Geant4 simulation of the mDOM used in this work has been developed by Lew Classen [4] and Björn Herold [6] and supplemented by Martin Unland [19]. Geant4 is a software toolkit implemented in C++ simulating the interactions of particles with matter based on Monte-Carlo methods [28]. The user can create geometrical volumes and assign materials and physical properties to them, define particle sources, track the particles as they pass through matter and detect them with sensitive detector geometries (for details see [33]). Informations on the tracked and detected particles can be retrieved from the simulation.

4.1. Geometry

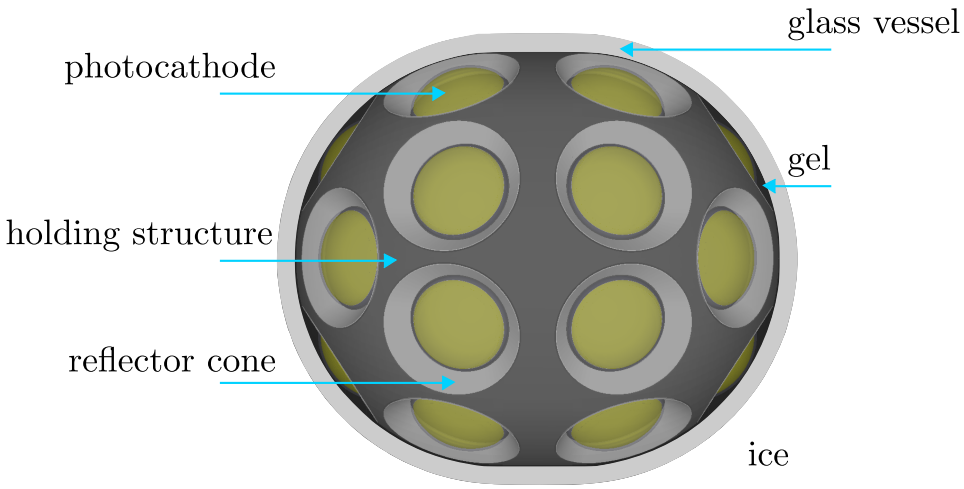

Figure 14: mDOM in the Geant4 simulation.

The geometry of the mDOM-simulation in Geant4 can be seen in Fig. 14. The geometrical structure is the same as described in Section 2.6. It can be chosen between different types of PMTs, reflectors, gels, vessel glasses and surrounding materials. In all the simulations done for this thesis the mDOM is deposited in ice with a Vitrovex glass vessel, silicone gel QGel900 from Quantum Silicones and Hamamatsu Photonics R12199 PMTs.

Correct handling of optical photons is taken care of by assigning refractive indices and the absorption lengths to the relevant materials, which are the ice, vessel glass, gel, PMT glass and photocathode. The PMT glass does not have an absorption length, it is incorporated in the quantum efficiency of the PMTs. The ice has an additional property describing Mie scattering. The optical properties of the ice in IceCube are depth dependent, but for the sake of simplicity they were chosen at a specific depth. The holding structure is completely absorbing, whereas the reflective cones reflect or absorb photons with a certain probability given by measurements. Except for the PMT glass and photocathode all mentioned properties are wavelength dependent.

4.2. Particles and Interactions

Table 2: Particles included in the Geant4 simulation of the mDOM, the physical processes they can participate in and the corresponding Geant4 classes.

Particle	**Physical process**	**Geant4 class**
Optical photon	Absorption	G4OpAbsorption
	Refraction and reflection at medium boundaries	G4OpBoundaryProcess
	Rayleigh scattering	G4OpRayleigh
	Mie scattering	G4OpMieHG
Gamma	Compton scattering	G4ComptonScattering
	Pair production	G4LivermoreGammaConversionModel
	Photoelectric effect	G4LivermorePhotoElectricModel
Electron/Positron	Scattering	G4eMultipleScattering
	Bremsstrahlung	G4eBremsstrahlung
	Ionisation	G4LivermoreIonisationModel
	Cherenkov radiation	G4Cerenkov
	Annihilation (only positron)	G4eplusAnnihilation
Alpha	Ionisation	G4ionIonisation
	Scattering	G4hMultipleScattering
Ion	Ionisation	G4ionIonisation
	Scattering	G4hMultipleScattering
	Radioactive Decay	G4RadioactiveDecay
All except optical photons	Scintillation	mdomScintillation

The particles and the interactions they can participate in are shown in Table 2. The class mdomScintillation is a modified version from M. Unland [19] of the G4Scintillation. The scintillation process is deactivated in the simulations done in the scope of this work. The reason is a bug occurring at small production cuts for secondary particles of electromagnetic energy loss processes. The production threshold can be given by the user as a length and is internally converted to a material dependent energy threshold [33].

4.3. From Primary Decay to PMT Response

For the studies on the mDOM calibration with radioactive decays the investigated isotopes are distributed randomly in the vessel glass. The isotopes decay instantly because the restricted number of unique representable values of float data types leads to decreasing time precision the longer the decay time becomes. The studies for the calibration are done only considering ^{40}K decays in the vessel glass, since this isotope is dominant in the analysed glass vessel.

The photocathode areas in the simulation are sensitive to photons in the range of 280 nm to 685 nm. As soon as a photon arrives at the photocathode, it is stopped and depending on the following analysis photon informations are written to a file. Only one decay is simulated at a time so the stored hits can be assigned to the respective decay and coincidences can be clearly identified. The coincidence time window is infinitely large in the simulation studies. The first detected photon from each decay has a hit time equal to zero and all following hit times are to be understood respectively to this first hit. Beside the hit time and the hit PMT of each detected photon, the identification number of the corresponding primary isotope, its position, the position of the photon production, of the reflections in the glass vessel and of its detection have been stored.

The PMT response has been added by M. Unland, of which only the the transit time spread feature has been used in this thesis. By default there is no relative time offset between the PMTs. The option of a wavelength dependent quantum efficiency was implemented by Cristian Lozano [34] and is used with the quantum efficiency seen in Fig. 15. It is an averaged QE based on multiple measurements of the Hamamatsu Photonics R12199.

At the end of this thesis a bug was found, because all photons are killed 100 ns after the decay. The bug is easy to debug but there was no time left to do it in the scope of this thesis. It is not expected that this bug has an important influence on the results of this thesis, since time difference distributions done with a simulation without that cutoff, but with other gel and without QE, show the same qualitative behaviour as the distributions shown in this thesis. A comparison of two exemplary plots can be seen in Fig. 57.

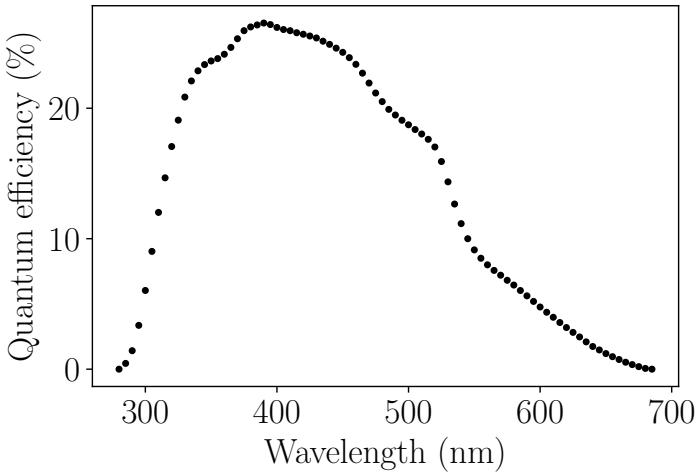

Figure 15: Quantum efficiency used in the Geant4 simulation as a weight to eliminate detected photons. It is based on the average from multiple measurements of the Hamamatsu Photonics R12199.

5. Simulation Studies on a Calibration Algorithm for the mDOM

In this chapter simulation studies are described in order to develop a calibration algorithm. The studies include hit and coincidence rates and hit time difference distributions with perfect and realistic time resolution. The coincidence rates and Δt-distributions with perfect time resolution lead to the choice of PMT combinations used for the calibration. The calibration is then performed with PMTs with different TTSs providing the time resolution.

Since the only isotope studied in the simulation is ^{40}K, a "decay" in this chapter denotes always a decay of ^{40}K.

5.1. Hit and Coincidence Rates

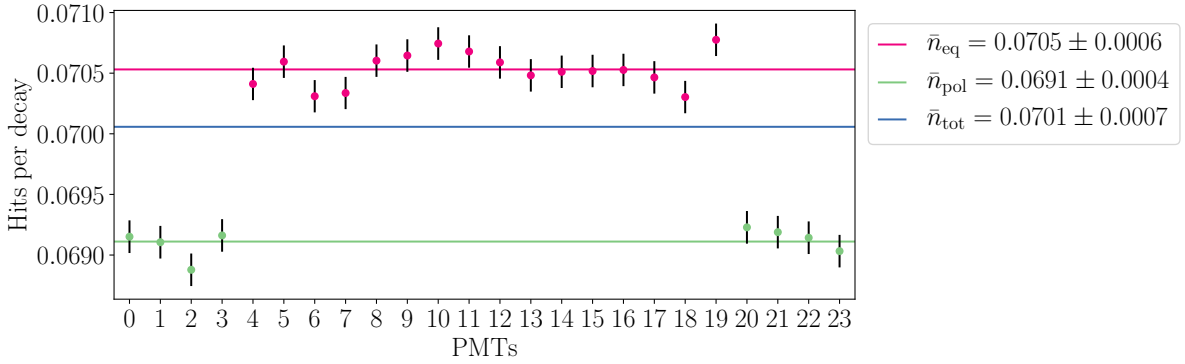

Figure 16: Mean number of hits per decay of all PMTs for the mDOM in ice. Equatorial PMTs and their average hit rate is shown in pink, polar PMTs and their average hit rate in green and the overall average in blue.

As already mentioned in Section 3.3 polar and equatorial PMTs have different hit rates, where hit rate means number of hits per decay. An illustration of polar and equatorial PMTs and the from now on used numbering of the PMTs can be seen in Fig. 20. Fig. 16 shows the hit rate for all PMTs. The mean of all PMTs is $\overline{n} = 0.0701 \pm 0.0007$ whereas the mean for polar PMTs and equatorial PMTs is $\overline{n}_{\mathrm{pol}} = 0.0691 \pm 0.0004$ and $\overline{n}_{\mathrm{eq}} = 0.0705 \pm 0.0006$ respectively.

The only difference between equatorial and polar PMTs in the simulation is the geometry of the module which therefore leads to the different hit rates. The PMT combinations in the mDOM can be divided into several subcategories depending on the symmetry of the combination, similar as there are two subcategories of PMTs when looking at single hits. Thus it is not surprising that the PMT combinations which differ in geometry also differ in their coincidence rates, as can be seen in Fig. 17. Coincidence rates are, analogue to

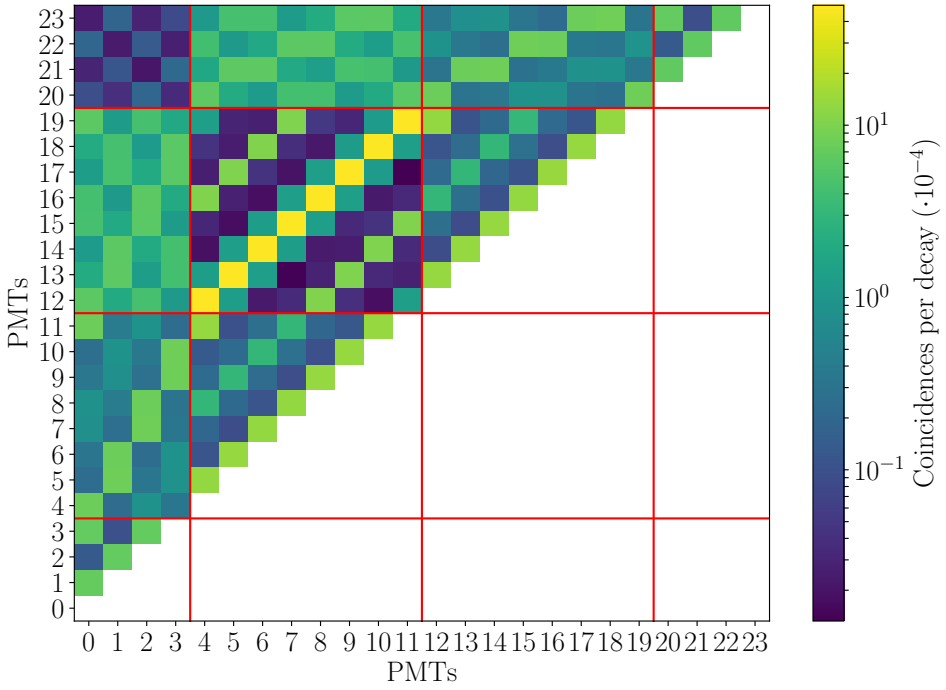

Figure 17: Number of coincidences per decay for all PMT combinations.

hit rates, defined as the number of coincidences per decays. The PMT combinations can be categorized by the type of the PMTs (equatorial - e or polar - p) and whether or not these lie in the same half vessel. These categories are separated in Fig. 17 by red lines. Beside this there is also a categorization depending on the angle between the PMTs. In Fig. 17 PMT combinations which are alike can be recognized as diagonal lines in the red boxes. For the KM3NeT DOMs an exponential decrease in the coincidence rates with increasing angular distance between the PMTs is observed, which is used in the calibration algorithm [23]. For the mDOM no dependency was found between the angle between the PMTs and the coincidence rate which could be used for the calibration, as can be seen in Fig. 18.

5.2. Hit Time Difference Distributions with Perfect Time Resolution

To investigate how the shapes of the hit time difference distributions (Δt-distributions) are generated (see Fig. 10 for an example from KM3NeT), the Δt-distributions are first calculated for PMTs with perfect time resolution by setting the TTS to zero. The simulated distributions show features appearing at different time scales, which are basically determined by the times photons are circling around the module inside the glass before their detection.

The connection between the Δt-distributions with and without TTS is given by the

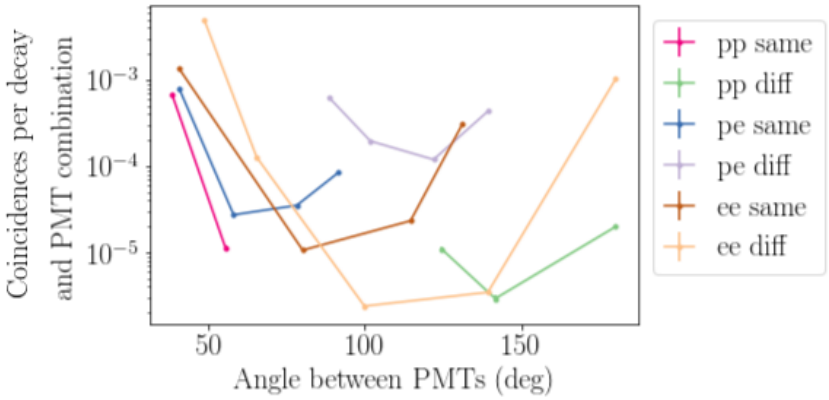

Figure 18: Coincidence rates depending on the angle between the PMTs. The rates are separated after PMT combination types and weighted with the occurrence of the types. "same" and "diff" indicate whether the PMTs lie in the same or different half vessel and "p" and "e" whether they are polar or equatorial. The angle is calculated with respect to the center of the mDOM.

convolution

$$f_{\mathrm{TTS}}(\Delta t) = f_{\mathrm{mDOM}}(\Delta t) * g(\Delta t; \mu, \sigma), \tag{12}$$

where $f_{\mathrm{TTS}}(\Delta t)$ is the Δt-distributions with TTS and $f_{\mathrm{mDOM}}(\Delta t)$ the Δt-distribution without TTS. The subscript "mDOM" indicates that the Δt-distribution without TTS is determined by the mDOM, to be precise by its geometry and the physical properties of its components. $g(\Delta t; \mu, \sigma)$ is a Gaussian with mean μ and standard deviation σ:

$$g(\Delta t; \mu, \sigma) = \frac{1}{\sqrt{2\pi\sigma^2}} \exp\left(-\frac{(\Delta t - \mu)^2}{2\sigma^2}\right). \tag{13}$$

The form of eq. (12) can be derived by inspecting the probability density function (pdf) of the sum of two independent random variables, which is given by the convolution of the pdfs of the two independent random variables. Here, three independent variables come into play: the transit times of the two PMTs and the hit time difference. The distribution of the transit times can be modeled by a Gaussian, as already mentioned in Section 2.3. The convolution of two Gaussians $g(\Delta t; \mu_i, \sigma_i)$ and $g(\Delta t; \mu_j, \sigma_j)$ is a Gaussian itself with

$$\mu = \mu_i + \mu_j \tag{14}$$

$$\sigma = \sqrt{\sigma_i^2 + \sigma_j^2}. \tag{15}$$

Here μ_i and μ_j are the time offset of PMTs i and j respective to a reference time. σ_i and σ_j equal the TTS of the respective PMTs. It is first naively assumed that $f_{\mathrm{TTS}}(\Delta t)$ can be described effectively by a Gaussian, similar to KM3NeT (in other words: it is

assumed that $f_{\mathrm{mDOM}}(\Delta t)$ can effectively be described by a Gaussian):

$$f_{\mathrm{TTS,eff}}(\Delta t) = \frac{A}{\sqrt{2\pi\sigma^2}} \exp\left(-\frac{(\Delta t-\mu)^2}{2\sigma^2}\right) \tag{16}$$

$$\mu = \mu_i + \mu_j \tag{17}$$

$$\sigma = \sqrt{\sigma_i^2 + \sigma_j^2} \tag{18}$$

$$A = A_{\mathrm{combi}} \cdot \epsilon_i \cdot \epsilon_j. \tag{19}$$

The amplitude A is differently defined in [23](KM3NeT) as the product of the PMT efficiencies ϵ_i and of a function depending on the angular distance between the PMTs. Instead of this function an amplitude A_{combi} is used here, which is equal for PMT combinations of the same type. μ_i is, as described before, the relative time offset to a reference PMT with $\mu_{\mathrm{ref}} = 0\,\mathrm{ns}$. σ_i is larger than the TTS in this effective description because of the width of the Δt-distribution without TTS. In order to find out whether this effective description is sufficient, the $f_{\mathrm{mDOM}}(\Delta t)$ of all PMT combinations are investigated. It should be noted that the following Δt-distributions are not pdfs since they are not normalized and were produced with limited statistics. But with increasing statistics their shape should approach the shape of the pdfs.

The Δt-distributions of the PMT combinations used for calibration should fulfill certain requirements in order to be able to apply the calibration algorithm using Gaussian fits as simply and accurately as possible. First of all, the higher the coincidence rate the better. As can be seen in Fig. 18, some combinations have coincidence rates several orders of magnitude lower than others. In order to keep the time needed for the calibration short, those with higher rates are preferred. Another criterion is whether the distributions have a dominant maximum at 0 ns, because otherwise the Gaussian would not be centered at 0 ns and an intrinsic offset would have to be introduced. These potential offsets could be determined by simulation studies, but they could introduce additional uncertainties. In addition the distributions should be symmetric around their maximum, since a Gaussian is also symmetrical.

There are 22 geometrically different PMT combinations in the mDOM. Fig. 19 shows the Δt-distributions for exemplary PMT combinations of these 22 combinations (see appendix A for all Δt-distributions). There are only three combinations with their global maximum at 0 ns, namely [0,1], [0,4] and [4,5]. These are not sufficient to calibrate the mDOM since there is no combination including PMTs from different half vessel. This would mean that a calibration of each half vessel separately is possible, but not of the whole module. The only combination with the same or higher coincidence rate as the other three combinations is [4,12], which would connect both half vessels. This combination has two maxima of the same height, which could potentially be problematic, but it is symmetric around 0 ns. All other PMT combinations which have amplitudes less than one order of magnitudes lower, feature one or two maxima which have larger offsets from 0 ns than the combination [4,12]. Therefore they would be less suitable to be fit with a

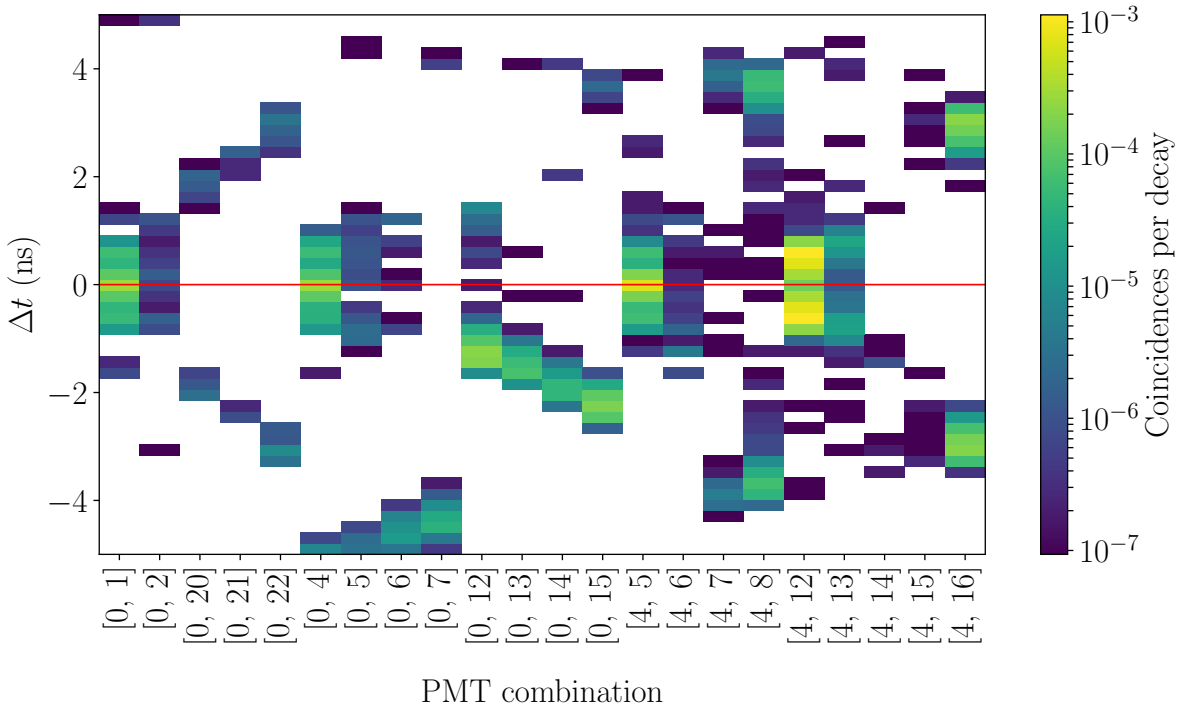

Figure 19: Exemplary Δt-distributions for each geometrically different PMT combination of the mDOM. The red line is at $\Delta t = 0\,\text{ns}$.

Gaussian.

The four combination types of [0,1], [0,4], [4,5] and [4,12] will be used for the calibration in the simulation and will from now on be called p-p (two polar PMTs in same vessel - [0,1]), p-e (polar and equatorial PMT in same vessel - [0,4]), e-e (two equatorial PMTs in same vessel - [4,5]) and e_1-e_2 (two equatorial PMTs in different vessels - [4,12]). All of these combinations are shown in Fig. 20.

5.2.1. Small Time Scales $< 1\,\text{ns}$

To interpret the following plots correctly, it is useful to know that the bulk contribution to a certain Δt comes from hit times smaller than that specific Δt, as can be seen in Fig. 21. The Δt-distributions for $\Delta t < 1\,\text{ns}$ for the four PMT combination types chosen for the calibration can be seen in Fig. 22. The three combinations p-p, p-e and e-e have their main peak at 0 ns. These are mainly photons being produced between the PMT, as is depicted in Fig. 23. Here a Mollweide projection of the mDOM is shown, where the PMTs are illustrated as gray ellipses. The mDOM projection is overlapped with a colormap illustrating the vertices of photons leading to coincidences in the two PMTs in lighter gray. A vertex is the point where a photon is produced. A cut was made on $-0.2\,\text{ns} \leqslant \Delta t \leqslant 0.2\,\text{ns}$ to get the decays leading to coincidences in the main peak for the PMT combinations [0,1], [0,4] and [4,5] representative for their combination types.

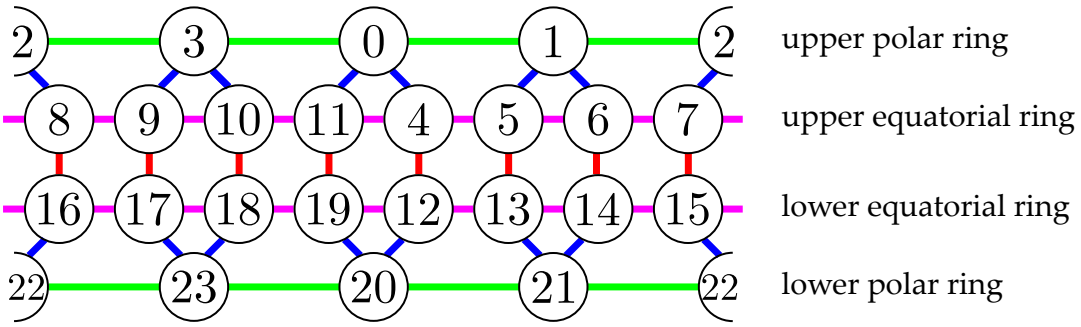

Figure 20: Projection of the mDOM with numbered PMTs. The lines mark combinations chosen for the calibration, the colors indicate different types of combination: green for p-p, blue for p-e, pink for e-e and red for e_1-e_2.

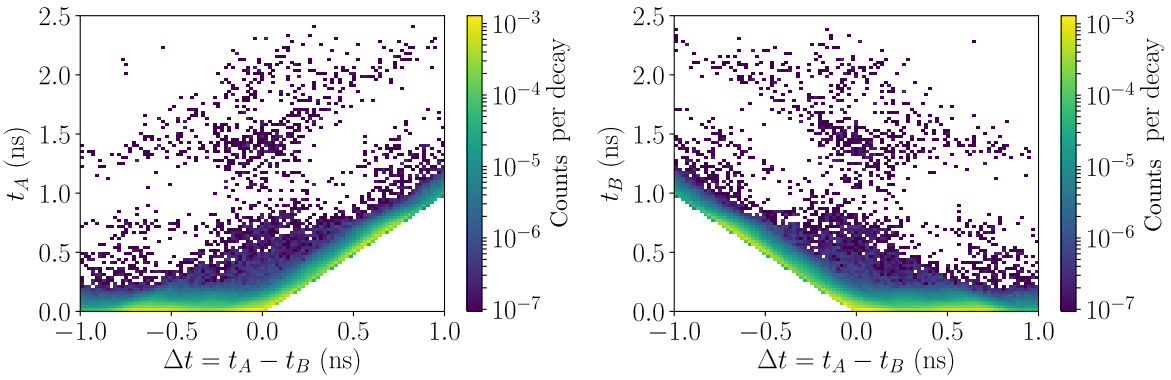

Figure 21: Occurrence of coincidences between PMT A and B depending on the hit times t_A, t_B and the hit time difference $\Delta t = t_A - t_B$. A and B are not specific, single PMTs, but they represent the sum of all PMT combinations. One hit time can contribute to multiple time differences.

The combination e_1-e_2 has no main peak at 0 ns but two equally high peaks symmetrically arranged around 0 ns. For this type the vertices of photons contributing to the main peaks are directly above the PMTs as can also be seen in Fig. 23, here represented by [4,12]. For this pair a cut was made on $-0.7\,\text{ns} \leqslant \Delta t \leqslant -0.4\,\text{ns}$. For vertices contributing to the right peak, the histogram has to be mirrored at the horizontal line between the PMTs. The reason for these two peaks is the greater distance between the PMTs. It leads to larger incident angles (with reference to the perpendicular) on the optical surfaces above the PMT for photons coming from the middle between the PMTs compared to PMTs closer together. Fig. 24 shows the positions of reflections at the glass-gel or glass-ice interfaces of photons contributing to coincidences. These histograms suggest that the photons are created above either of the PMTs and partly hit it while others get reflected once between the PMTs at the glass-ice surface and then hit the other one.

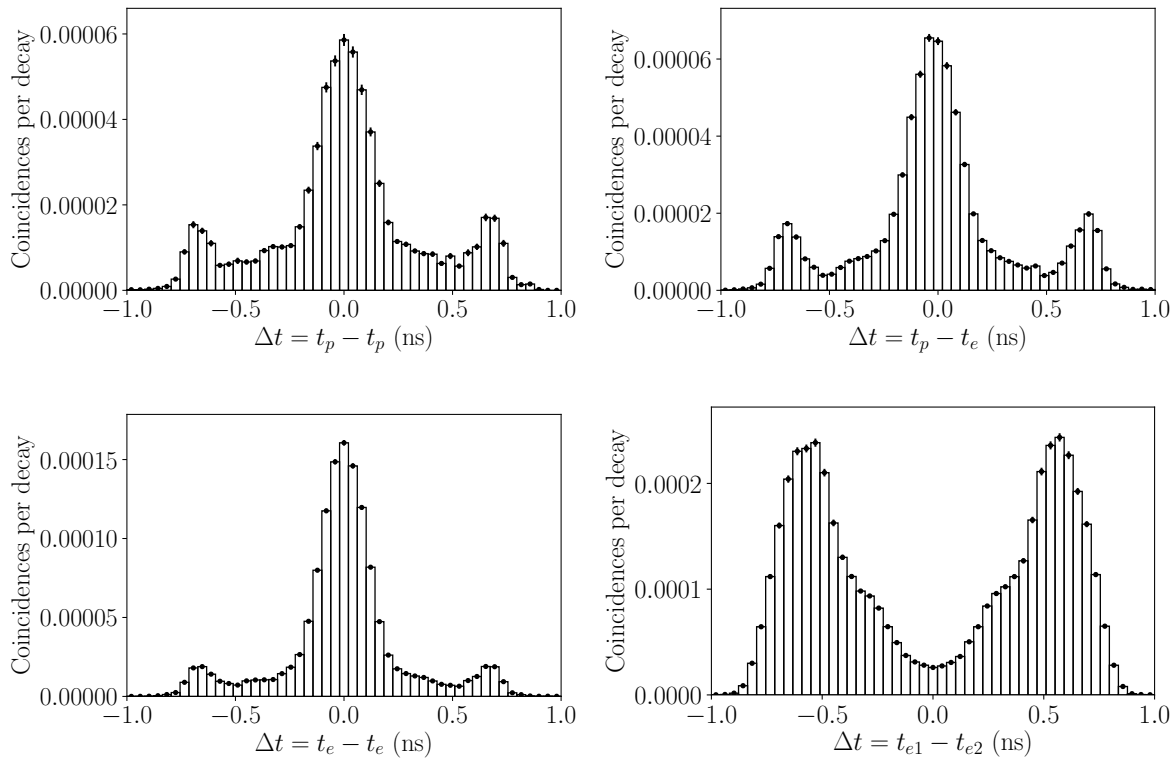

Figure 22: Δt-distribution for the PMT combination types used for the calibration with PMTs with TTS= 0 ns for small time scales. The coincident rates are the sum of the rates of all PMT combinations of the same type normalized by the occurrence of the types.

The smaller peaks at each side of the main peaks of p-p, p-e and e-e originate partly from the reflector cone surrounding the PMTs, but cannot be fully explained by them. In addition the reflectors are broadening the main peaks of all PMT combination types. The comparison between Δt-distributions from a simulation with normal reflective cones and totally absorbing cones can be seen in appendix A. The other factor contributing to these peaks is probably given by photons getting reflected once before hitting the PMT, which is the same effect that leads to the two main peaks for the e_1-e_2 combinations. Fig. 25 shows exemplarily the photon vertices and reflection points of photons contributing to $-0.8\,\text{ns} \leqslant \Delta t \leqslant -0.6\,\text{ns}$ for the PMTs [4,5]. This corresponds to the side peak where PMT 4 is hit before PMT 5. Photons contributing to that side peak are produced at the side of PMT 4 pointing away from PMT 5 and then get reflected once between the PMTs before hitting PMT 5.

5.2.2. Large Time Scales

The Δt-distributions for larger time scales are shown in Fig. 26. All PMT combination types show different behaviour. This is because photons traveling around the whole mo-

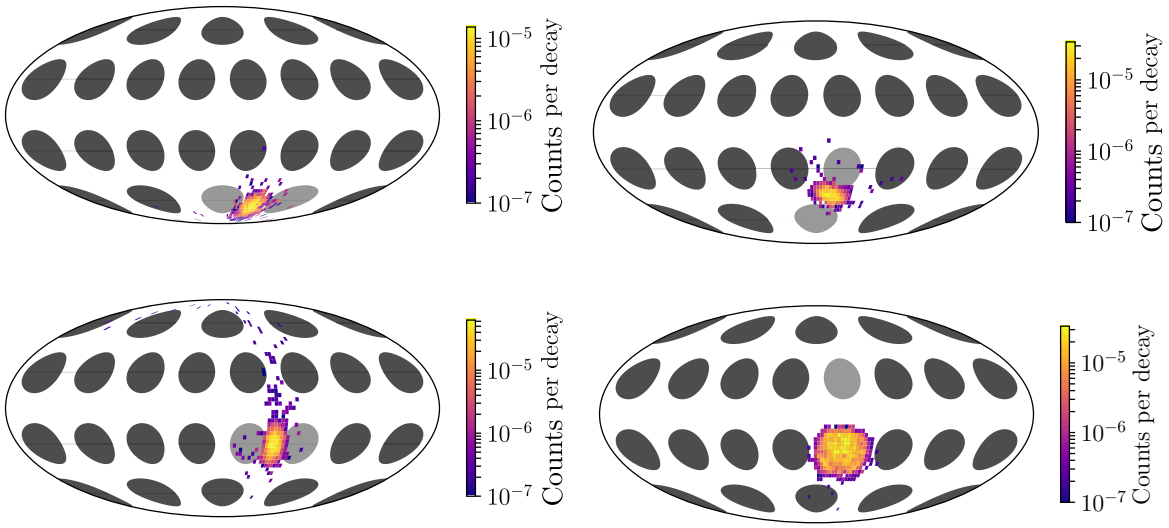

Figure 23: Mollweide projection of the mDOM with gray ellipses illustrating the PMTs and an 2d histogram of vertices of photons contributing to twofold coincidences on the two lighter PMTs. Cuts for [0,1] (upper left), [0,4] (upper right) and [4,5] (lower left): $-0.2\,\text{ns} \leqslant \Delta t \leqslant 0.2\,\text{ns}$. Cut for [4,12] (lower right): $-0.7\text{ns} \leqslant \Delta t \leqslant -0.4\,\text{ns}$, corresponding to the left peak, where PMT 4 was hit first.

dule get affected by the geometric asymmetry of the mDOM, and not only by the local geometry between two PMTs. The frequently repeating maxima, which are more or less distinct depending on the combination type, mark one or several circuits of the module by a photon before hitting a PMT. The circumference at the outside of the glass vessel at the long axis is about 1.23 m corresponding to a time of 6.06 ns when traveled with the speed of light in glass. The circumference at the inside of the glass vessel along the short axis is about 1.04 m corresponding to 5.11 ns. These two values shall serve as an estimation for how long photons need to circulate around the module once and they and their duplicate and triple are marked in Fig. 26 as green areas. The maximas tend to lie at slightly larger time differences, which is due to reflections lengthening the path.
The coincidence rate is expected to decrease with the distance traveled by the photons due to absorption in the glass and transmission into the ice or gel, leading to a decrease in amplitude of successive maxima.
Apparently, polar PMTs are less likely to be hit by photons circulating around the module than equatorial PMTs are, due to their geometrical differences. The Δt-distribution of two equatorial PMTs of the same ring shows nearly equal heights of the second and third side maximum in contradiction to the Δt-distributions of the other two combinations including equatorial PMTs. The exact reason for this was not found, but a striking difference to the other PMT combinations is that the connection line between the PMTs of the e-e combination is along the short axis of the module whereas the other combinations including equatorial PMTs have their connection line along the long axis.

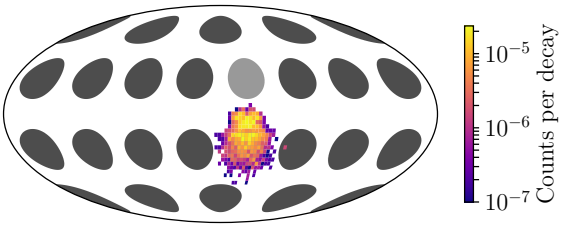

Figure 24: Mollweide projection of the mDOM with gray ellipses as PMTs and an 2d histogram of reflection points at the glass-gel or glass-ice surface of photons contributing to twofold coincidences on the two lighter PMTs, namely PMTs [4,12]. Cuts have been made on $-0.7\,\text{ns} \leqslant \Delta t \leqslant -0.4\,\text{ns}$ corresponding to the left peak, where PMT 4 was hit first.

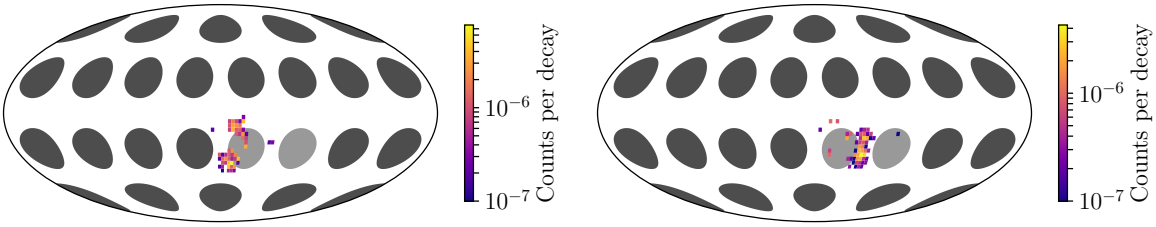

Figure 25: Mollweide projection of photon vertices (left) and reflection points (right) of photons contributing to $-0.8\,\text{ns} \leqslant \Delta t \leqslant -0.6\,\text{ns}$ for PMTs [4,5], corresponding to the side peak where PMT 4 is hit first.

The question to take from this is whether the asymmetry of the p-e distributions interferes with the calibration method, since a Gaussian is symmetric. This will be studied in the next section.

5.3. Calibration Algorithm and Results

The calibration is tested with PMTs with different transit time spreads of 0.5 ns, 1 ns and about 1.7 ns. In the following simulation studies it is assumed that all PMTs have the same TTS that is constant. The figs. 28 to 30 show the time difference distributions for different TTSs. The main peak has no substructure for any of the investigated TTS. Of course it might be possible that for lower TTS the substructures are resolved, especially at the combination e_1-e_2, because of the two equally high main peaks. For 0.5 ns the maxima from the photons circulating around the module can be distinguished from one another, but with larger TTS the distribution gets more smeared and at 1.7 ns there is only one maximum left. A Gaussian describes the distributions well except for the p-e combinations, because of their asymmetry.

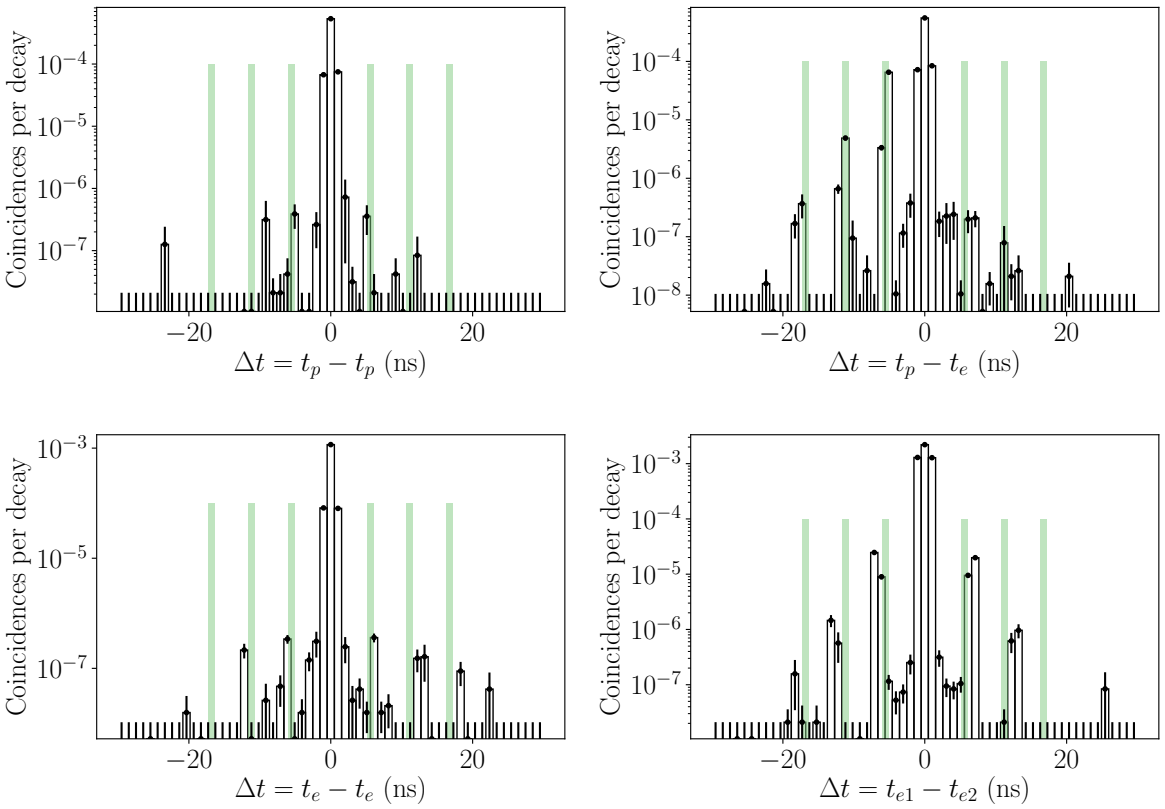

Figure 26: Δt-distribution for the PMT combination types used for the calibration with PMTs without TTS for large time scales. The coincident rates are the sum of the rates of all combinations of the same type normalized by the frequency of the types. The green areas are the roughly estimated circling times for a photon around the module in the glass.

The calibration is done using an global fit, as described in Section 3.2. PMT 0 is used as reference PMT with no time offset: $\mu_0 = 0\,\text{ns}$. All other μ_i describe the relative time offset of PMT i to PMT 0. If all other parameters of Section 5.2 are free to be varied by the fit, all parameters influencing the amplitude A have infinite or very large uncertainties (the four A_{combi} and the 24 ϵ_i). In addition the Gaussian model does not fit the simulated data points well for some PMT combinations because the amplitude is too high or too low, as can be seen in Fig. 27. Because of this complications, from this point on the fit function contains only one effective amplitude A for each PMT combination and the focus will be on the time calibration of the mDOM.

The problem with the amplitudes which are not fitting the data still consist with one effective amplitude for each Δt-distribution. The solution is to introduce an additional term to σ which is the same for all PMT combinations of the same type:

$$\sigma = \sqrt{\sigma_i^2 + \sigma_j^2 + \sigma_{\text{combi}}^2}. \tag{20}$$

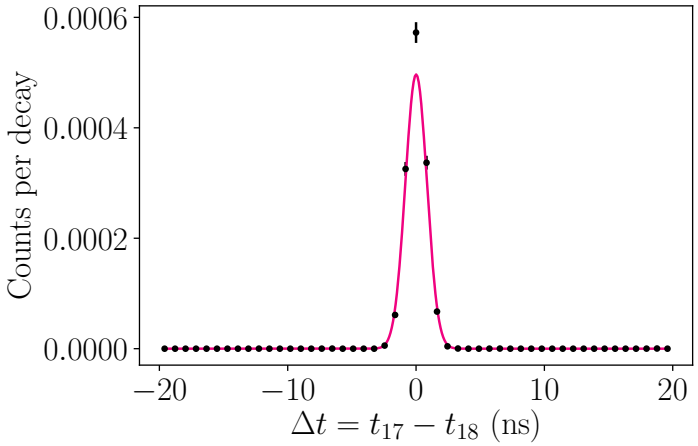

Figure 27: Δt-distribution of PMT 17 and 18 with TTS = 0.5 ns. Fitted in an global fit with Gaussian as in Section 5.2 with $\mu_0 = 0$ ns fixed. As all other Δt-distributions shown in this thesis this plot is a histogram although the bins are in this case not indicated by bars. The bins are also equally

This parameter ought to effectively take into account the different shapes of the Δt-distributions with perfect time resolution of the different PMT combination types. σ_{combi} is determined by holding all other parameters fixed except for the amplitudes and then introducing the fixed σ_{combi} in the normal fit. The determination of σ_{combi} is done for TTS= 0.5 ns since there the simple Gaussian fit works best, because the main peak is most distinguishable from the side peaks. The four σ_{combi} can be seen in Table 3.

Table 3: σ_{combi} for the four PMT combination types as determined from the Δt-distributions with TTS= 0.5 ns.

PMT combination type	σ_{combi}
p-p	0.414 ± 0.013
p-e	0.421 ± 0.009
e-e	0.362 ± 0.007
e_1-e_2	0.548 ± 0.005

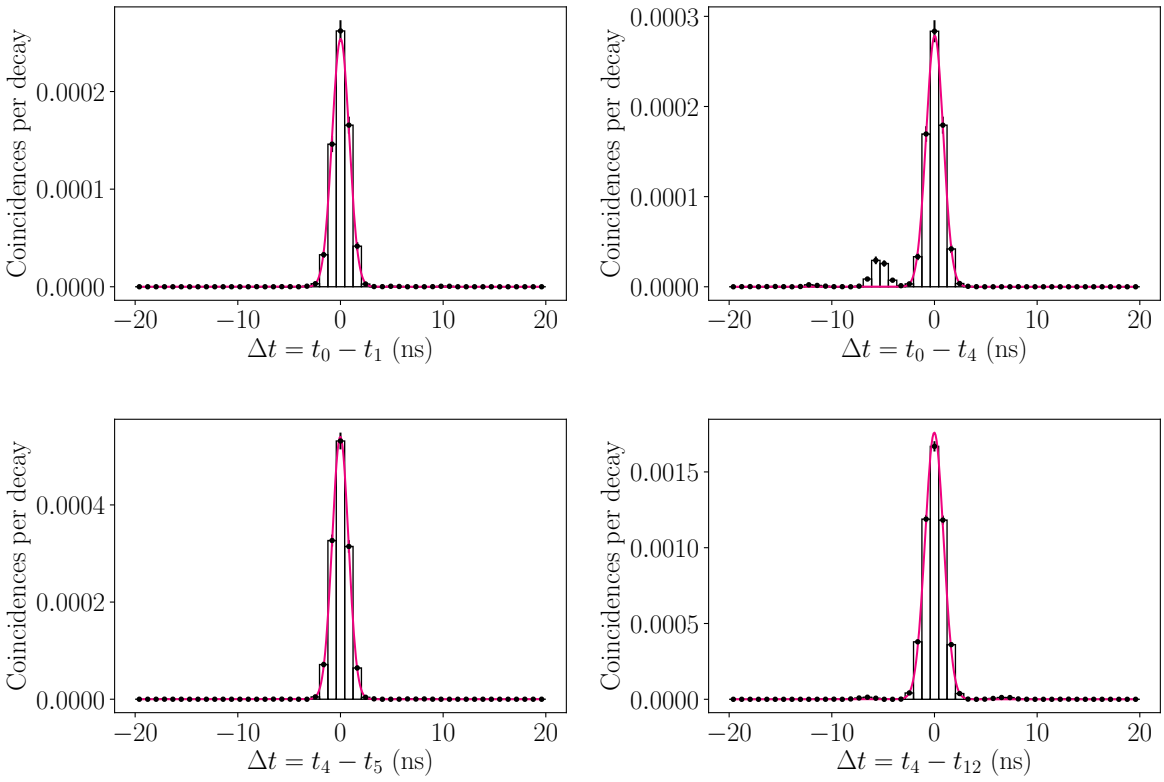

Figure 28: Δt-distribution and global fit with σ_{combi} fixed for the PMT combinations exemplary for the types used for the calibration with TTS = 0.5 ns.

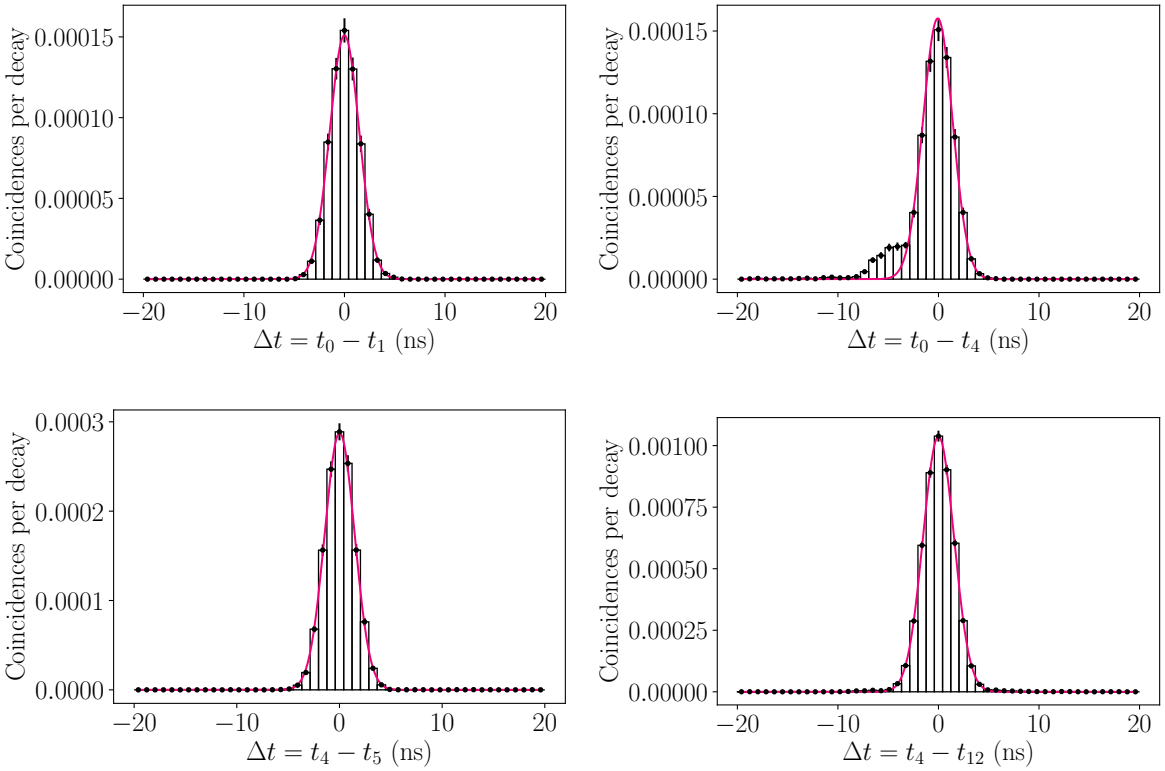

Figure 29: Δt-distribution and global fit with σ_{combi} fixed for the PMT combinations exemplary for the types used for the calibration with TTS = 1 ns.

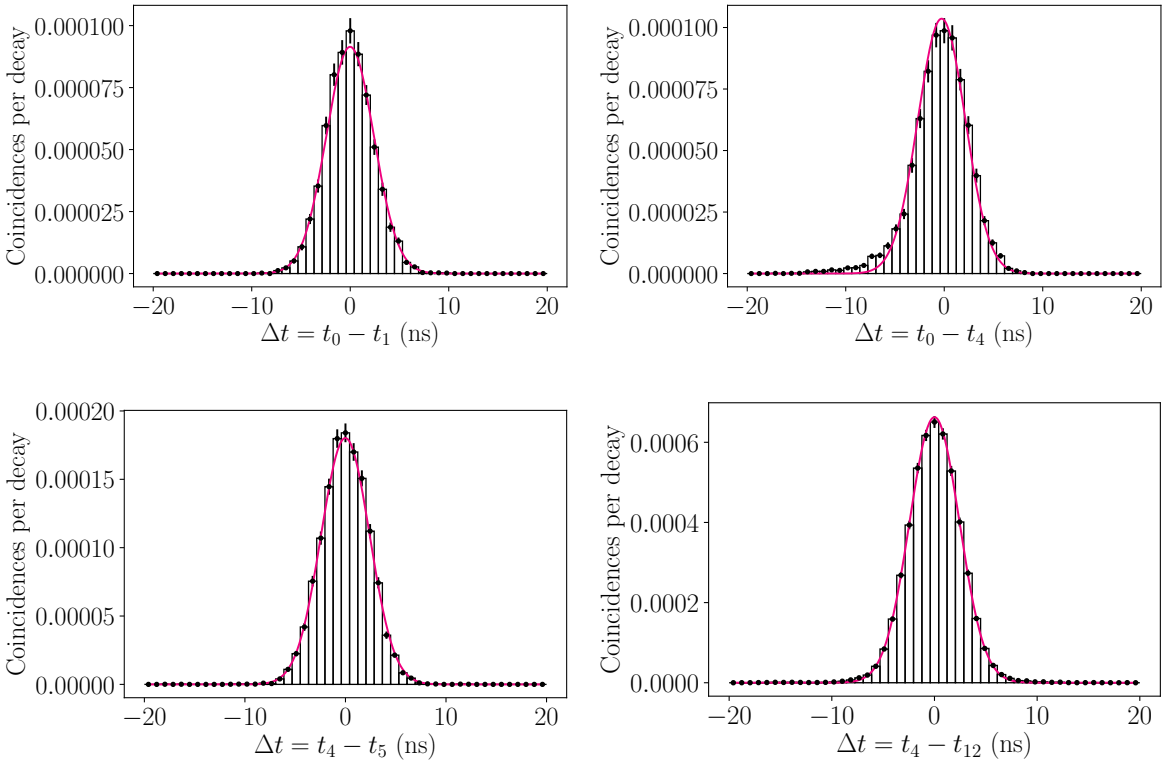

Figure 30: Δt-distribution and global fit with σ_{combi} fixed for the PMT combinations exemplary for the types used for the calibration with TTS $\approx 1.7\,\text{ns}$.

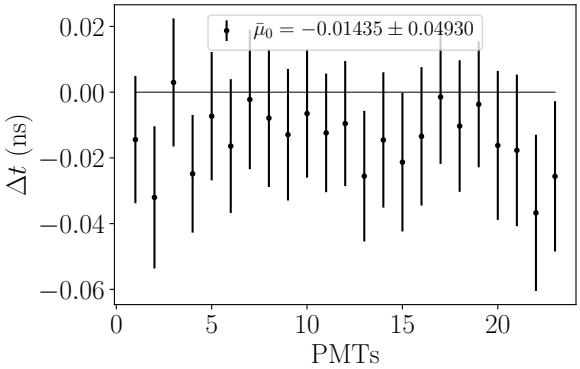

Figure 31: Relative time offsets from the global fit with σ_{combi} fixed for all PMTs with TTS $= 0.5\,\text{ns}$.

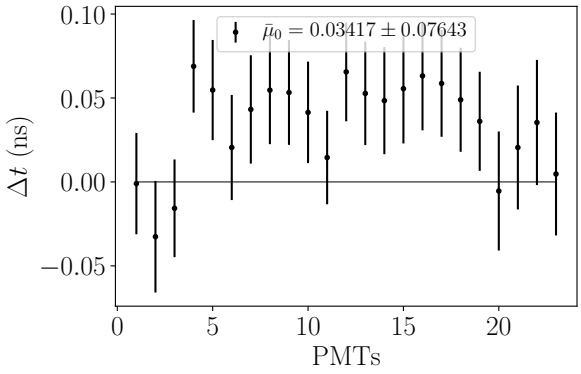

Figure 32: Relative time offsets from the global fit with σ_{combi} fixed for all PMTs with TTS = 1 ns.

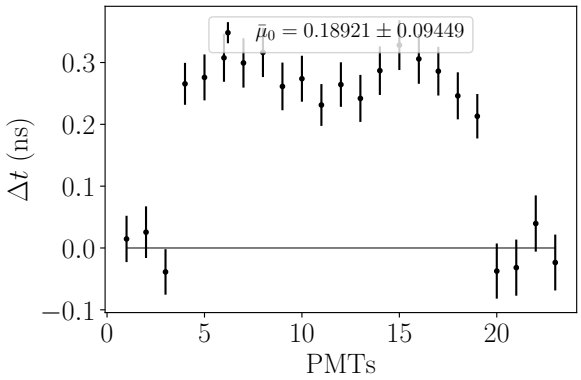

Figure 33: Relative time offsets from the global fit with σ_{combi} fixed for all PMTs with TTS ≈ 1.7 ns.

Examples for each combination type for the global fit with fixed σ_{combi} can be seen in Fig. 28. There is still a feature in the amplitudes of the e_1-e_2 combinations: they are slightly too high at the maximum. This could be a feature of the two equally high main peaks this combination shows without TTS, which could cause a flat-toped maximum. The relative time offsets for TTS= 0.5 ns can be seen in Fig. 31. Nearly all time offsets are slightly negative, which could be an artifact of the asymmetric p-e distributions. At larger TTSs the relative time offsets deviate stronger from 0 ns, as can be seen in Fig. 32 and Fig. 33. Here the polar PMTs have offsets equal to 0 ns, but the equatorial PMTs have significant positive offsets, increasing for larger TTS. This reflects the fact that for the p-e combinations the mean of the Gaussian is at $\mu = \mu_{\text{p}} - \mu_{\text{e}}$ and the mean of the Gaussian is shifted to negative time differences, as can be seen in Fig. 29 and Fig. 30. For TTS$\approx$ 1.7 ns the maximal offset from 0 ns is below 0.37 ns, for TTS= 1 ns it is below 0.10 ns.

Two approaches have been made to eliminate the offset, but both were not completely successful. The problem is obviously the p-e combinations, whose fit function is therefore changed. The first approach was to fit also a Gaussian to the first maximum and to the first two maxima at negative time differences. The one/two additional Gaussians were fitted to the time difference distributions at 0.5 ns, were their means were determined by fixing the mean and sigma of the main peak of all PMT combinations with $\mu_i = 0$ ns and $\sigma_i = 0.5$ ns and forcing the means, amplitudes and σ of the additional Gaussians to be at the same position for all p-e combinations. The resulting mean for one additional Gaussian is (-5.289 ± 0.014) ns, the means for the two additional Gaussians are (-5.289 ± 0.013) ns and (-11.61 ± 0.06) ns. The position of the first side maximum is the same in both cases, as was to be expected. They are also in good agreement with the interval of 5.11 ns to 6.06 ns used to estimate the time a photon needs to circle the module once in the glass. The double of this estimated interval would reach from 10.22 ns to 12.12 ns, which is also in agreement with the position of the second side maximum at -11.61 ns. The results of the global fit for one additional Gaussian with its mean fixed and all other parameter free (except for the reference time) can be seen in figs. 34 to 39. The results of the global fit for two additional Gaussian with their means fixed can be seen in figs. 40 to 45. There is not a large difference between using one or two additional Gaussians. For TTS$\approx$ 1.7 ns the offset is reduced to below 0.14 ns with one Gaussian and below 0.15 ns with two Gaussians. For TTS= 1 ns the offset is reduced to below 0.08 ns in both cases.

The second approach is to fit a Gaussian convoluted with an exponential to the distribution of TTS= 1.7 ns. This idea was developed by looking at the Δt-distribution of the p-e combinations with PMTs without TTS. Fig. 46 shows this distribution with an exponential fit of the main peak and the three first side maxima for negative time differences, which fits very well. Remember that the Δt-distribution with TTS should be equal to the convolution of the Δt-distribution without TTS and a Gaussian depending on the TTS of the two PMTs. The ansatz here is that for large TTS the gaps between the maxima in the Δt-distribution without TTS are not relevant any more and only the

envelope is important, which is given by an exponential for negative time differences. The developed fit function is a convolution of a Gaussian $g(\Delta t)$ and an exponential function restricted to negative time differences $f(\Delta t)$ with

$$g(\Delta t) = \frac{A_{\text{eff}}}{\sqrt{2\pi\sigma^2}} \exp\left(-\frac{(\Delta t - \mu)^2}{2\sigma^2}\right) \tag{21}$$

$$f(\Delta t) = \exp(\lambda \cdot \Delta t) \text{ for } \Delta t \leqslant 0 \tag{22}$$

$$f(\Delta t) = 0 \text{ for } \Delta t > 0, \tag{23}$$

where $\lambda > 0\,\text{ns}^{-1}$. μ and σ are defined as in Section 5.2 and eq. (20) respectively and A_{eff} is the introduced effective amplitude different for each PMT combination. The convolution of these two functions is given by

$$\frac{A_{\text{eff}}}{2} \cdot \exp\left(\frac{\lambda}{2}(\lambda\sigma^2 + 2\Delta t - 2\mu)\right) \cdot \left(2 - \text{erfc}\left(\frac{-\lambda\sigma^2 + \mu - \Delta t}{\sqrt{2}\sigma}\right)\right), \tag{24}$$

where erfc is the complementary error function

$$\text{erfc}(x) = 1 - \text{erf}(x) = \frac{2}{\sqrt{\pi}} \int_x^\infty e^{-t^2}\, dt. \tag{25}$$

This convolution is used as the fit function for the p-e combinations. It is tested only for TTS$\approx 1.7\,\text{ns}$, since there the smearing of the Gaussian is largest. The results can be seen in Fig. 47 and Fig. 48. The offset is not eliminated, but its magnitude is increased from $\approx 0.3\,\text{ns}$ to $\approx 1.1\,\text{ns}$ for the equatorial PMTs, although the fit function seems to describe the data better than a simple Gaussian.

Both approaches made to eliminate the offset did not fully succeed, although fitting additional Gaussian to the side maxima reduces it. Since the origin of the offset is given by $f_{\text{mDOM}}(\Delta t)$ incorporating the geometry and physical properties of the module it should be able to determine the offsets with high accuracy with simulations. Fluctuations in material and geometry properties in the production of mDOMs could lead to uncertainties, which could in principle be also investigated with simulation studies.

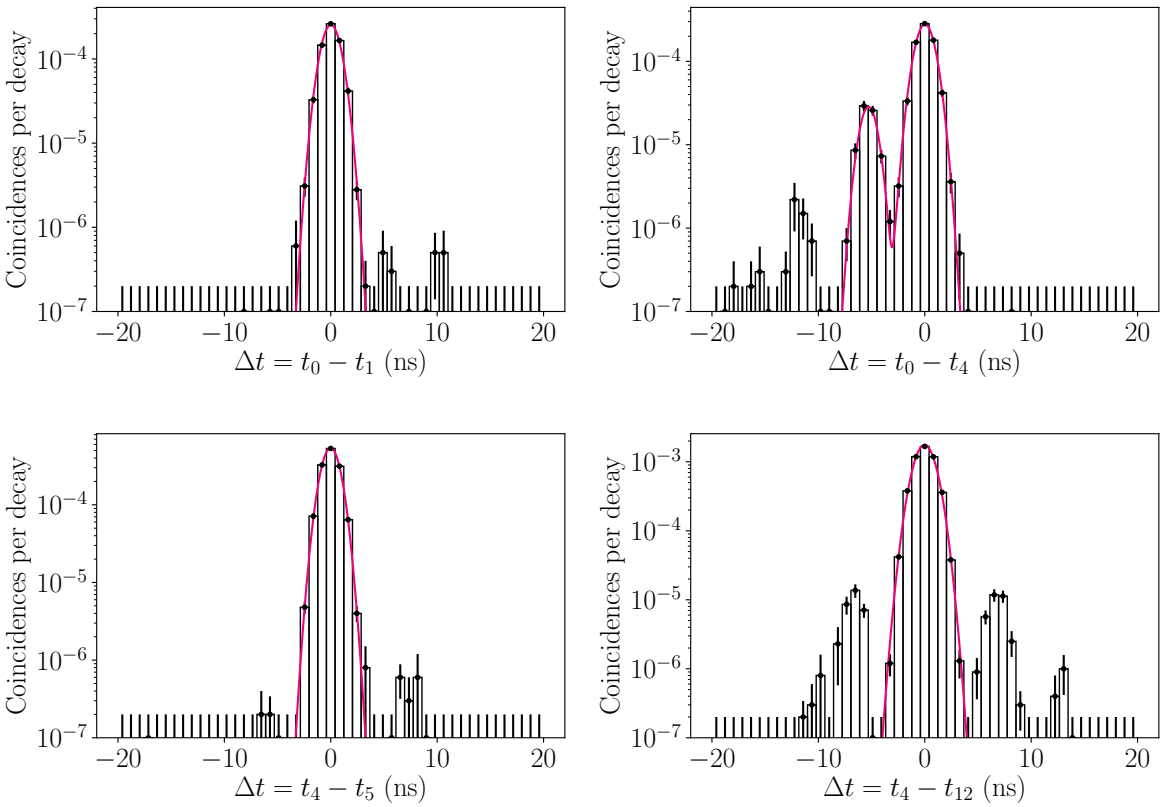

Figure 34: Δt-distribution and global fit with σ_{combi} fixed and one additional Gaussian with fixed mean for p-e combinations for the PMT combinations exemplary for the types used for the calibration with TTS = 0.5 ns.

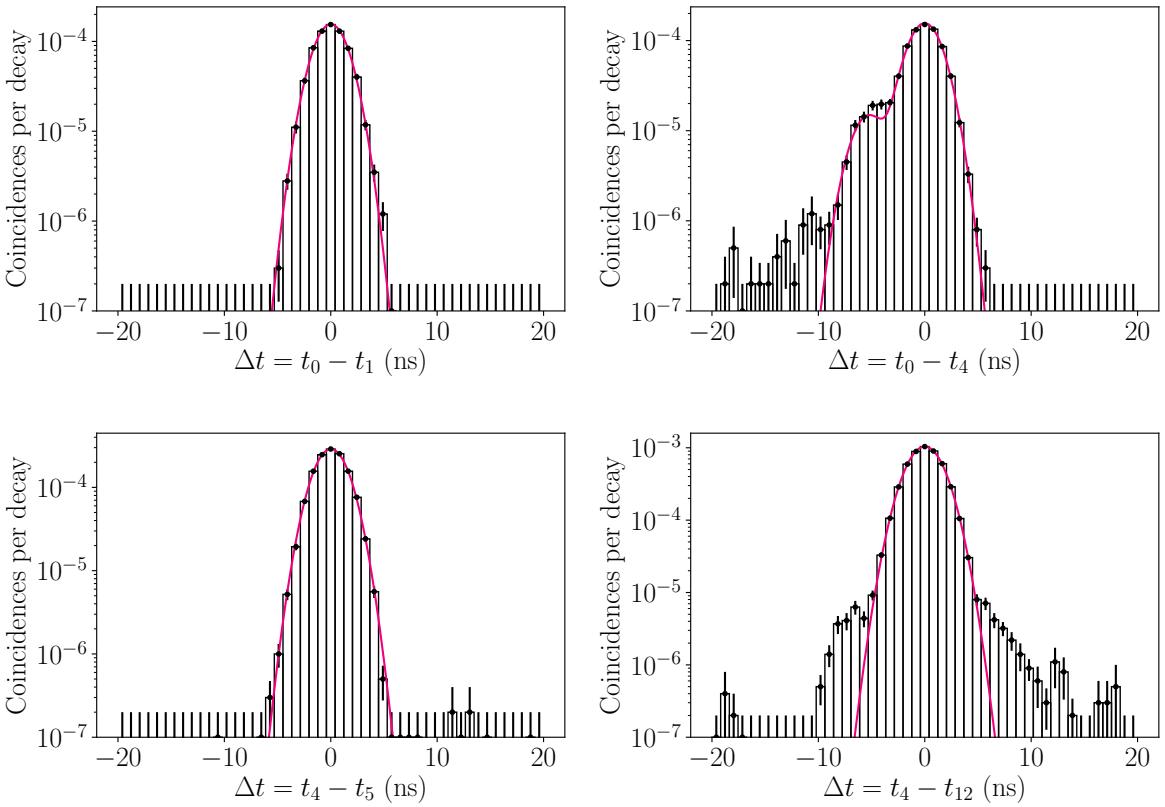

Figure 35: Δt-distribution and global fit with σ_{combi} fixed and one additional Gaussian with fixed mean for p-e combinations for the PMT combinations exemplary for the types used for the calibration with TTS = 1 ns.

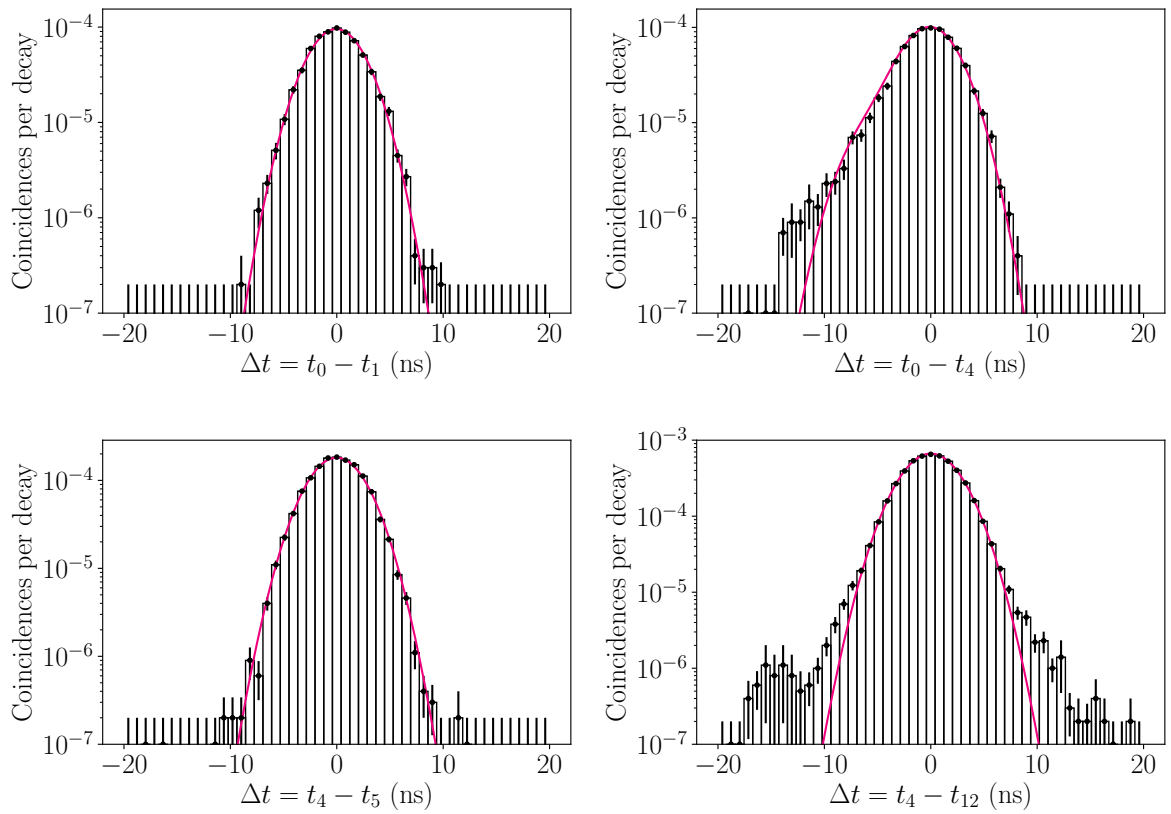

Figure 36: Δt-distribution and global fit with σ_{combi} fixed and one additional Gaussian with fixed mean for p-e combinations for the PMT combinations exemplary for the types used for the calibration with TTS $\approx 1.7\,\text{ns}$.

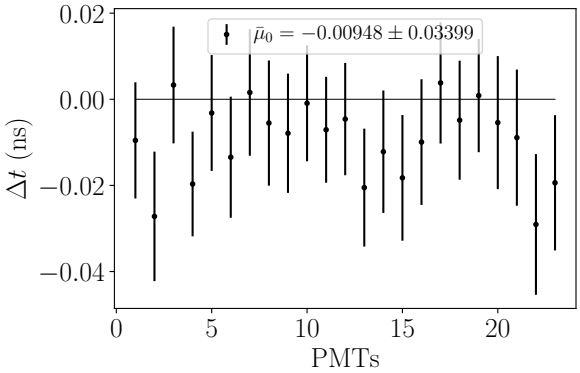

Figure 37: Relative time offsets from the global fit with σ_{combi} fixed and one additional Gaussian with fixed mean for p-e combinations for all PMTs with TTS = 0.5 ns.

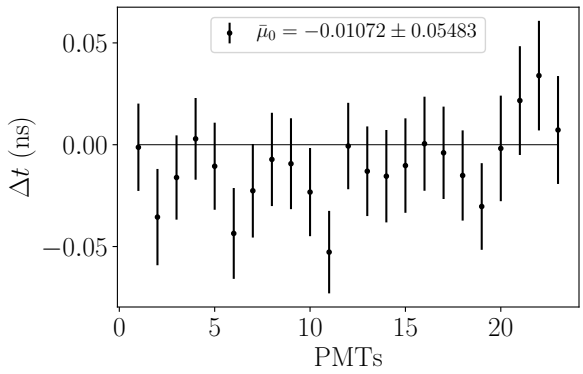

Figure 38: Relative time offsets from the global fit with σ_{combi} fixed and one additional Gaussian with fixed mean for p-e combinations for all PMTs with TTS = 1 ns.

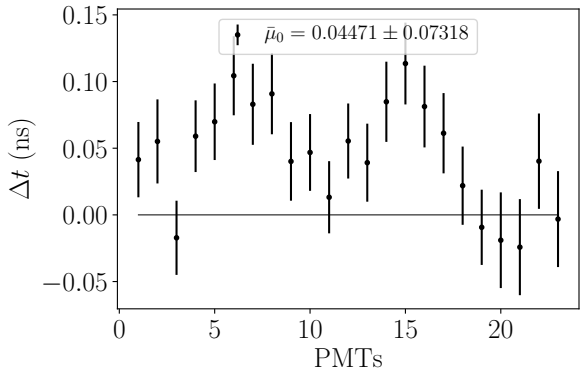

Figure 39: Relative time offsets from the global fit with σ_{combi} fixed and one additional Gaussian with fixed mean for p-e combinations for all PMTs with TTS $\approx$ 1.7 ns.

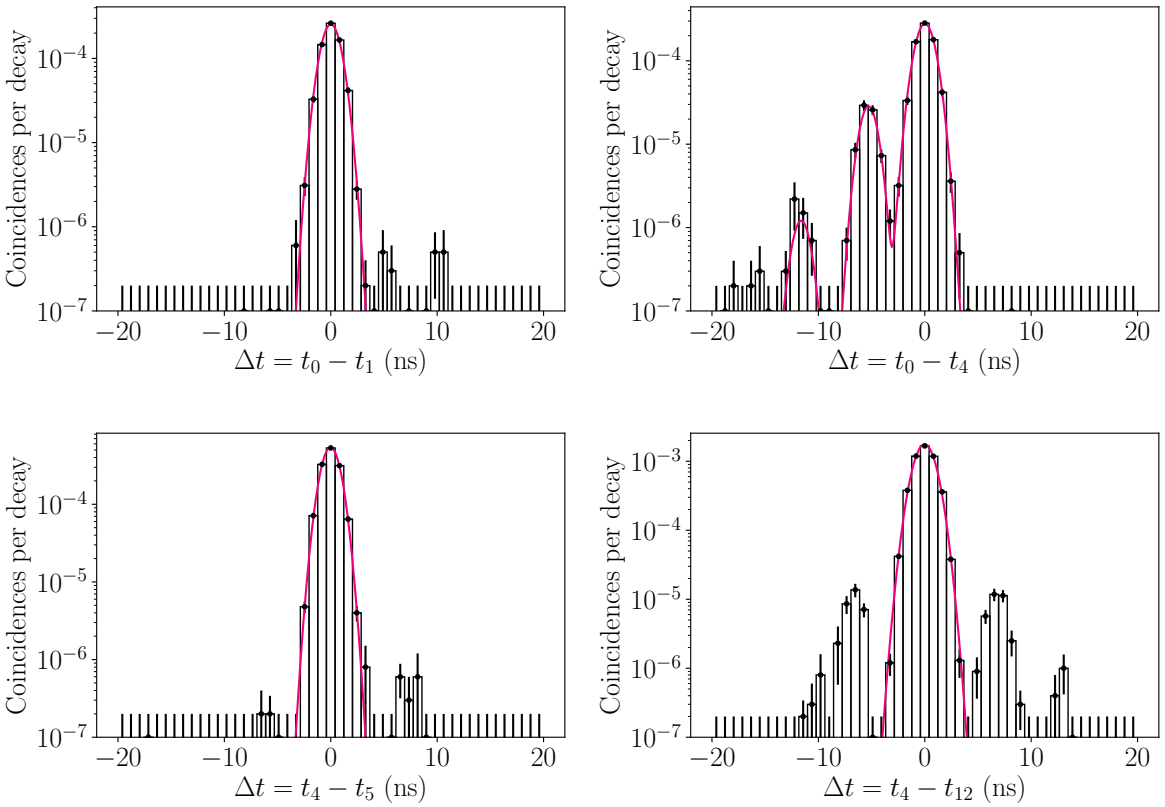

Figure 40: Δt-distribution and global fit with σ_{combi} fixed and two additional Gaussians with fixed means for p-e combinations for the PMT combinations exemplary for the types used for the calibration with TTS = 0.5 ns.

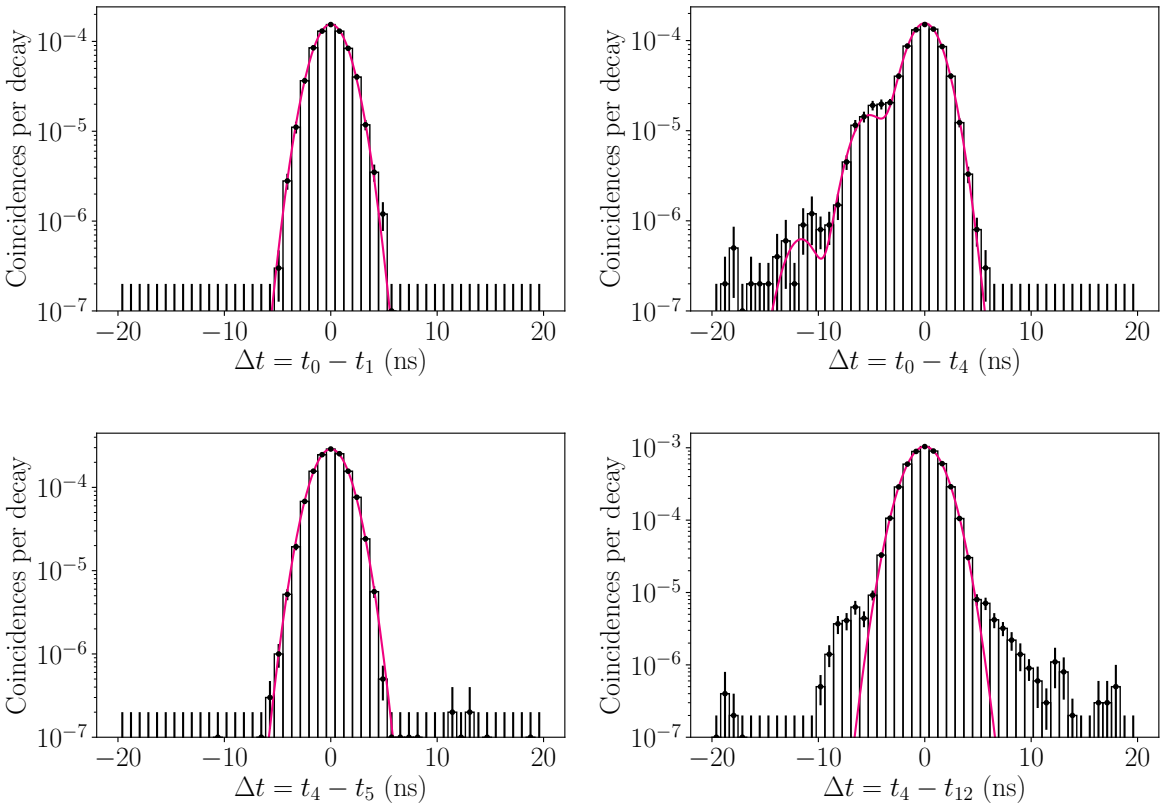

Figure 41: Δt-distribution and global fit with σ_{combi} fixed and two additional Gaussians with fixed means for p-e combinations for the PMT combinations exemplary for the types used for the calibration with TTS = 1 ns.

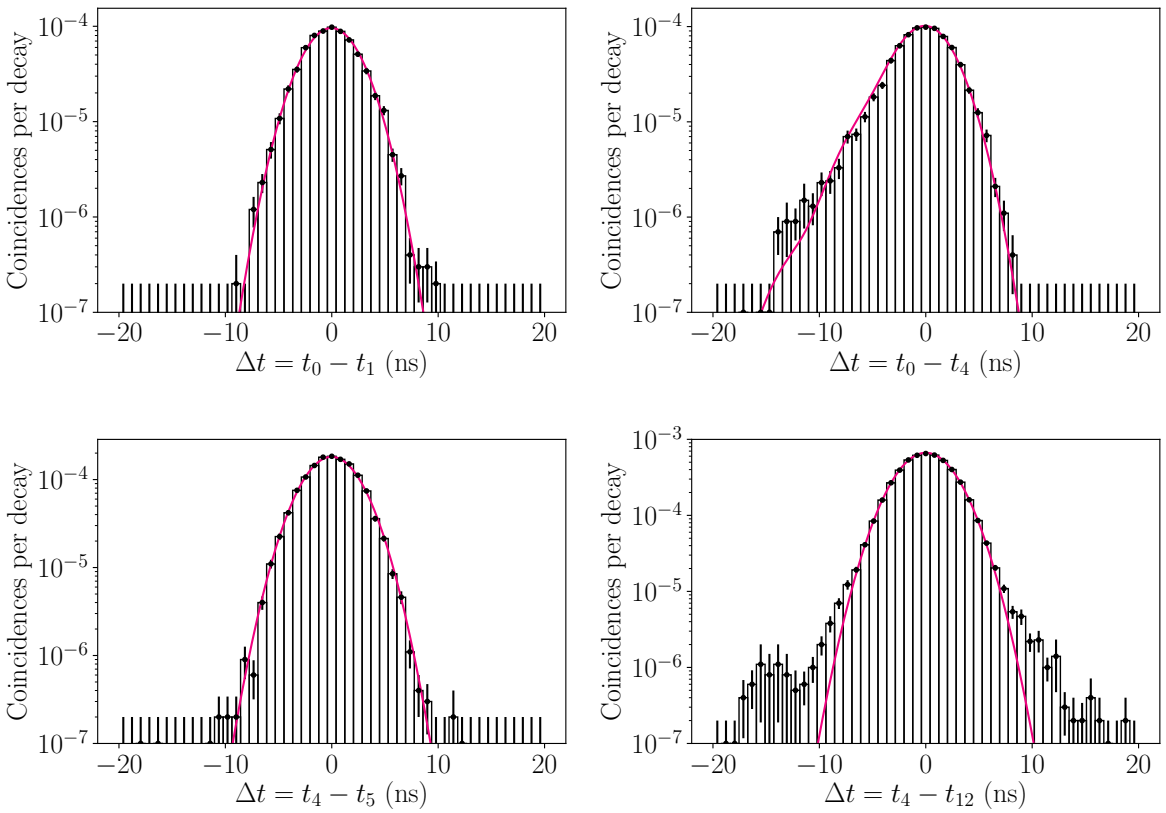

Figure 42: Δt-distribution and global fit with σ_{combi} fixed and two additional Gaussians with fixed means for p-e combinations for the PMT combinations exemplary for the types used for the calibration with TTS $\approx 1.7\,\text{ns}$.

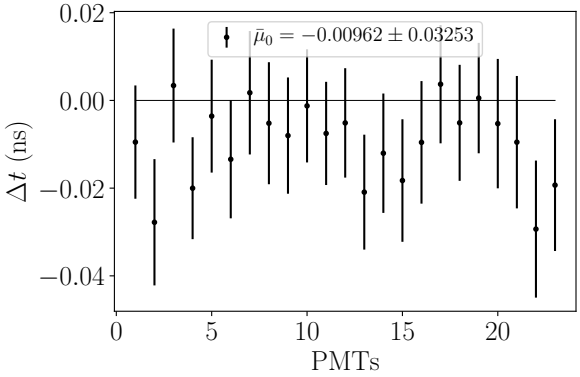

Figure 43: Relative time offsets from the global fit with σ_{combi} fixed and two additional Gaussians with fixed means for p-e combinations for all PMTs with TTS = 0.5 ns.

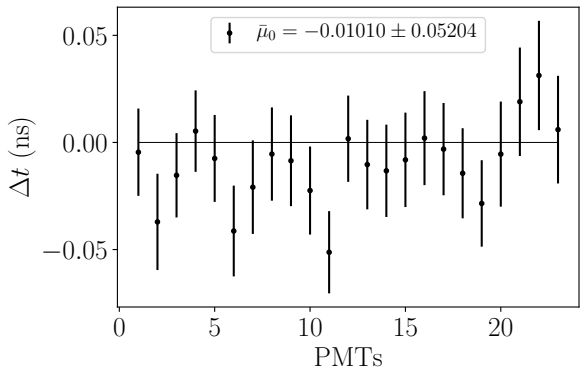

Figure 44: Relative time offsets from the global fit with σ_{combi} fixed and two additional Gaussians with fixed means for p-e combinations for all PMTs with TTS = 1 ns.

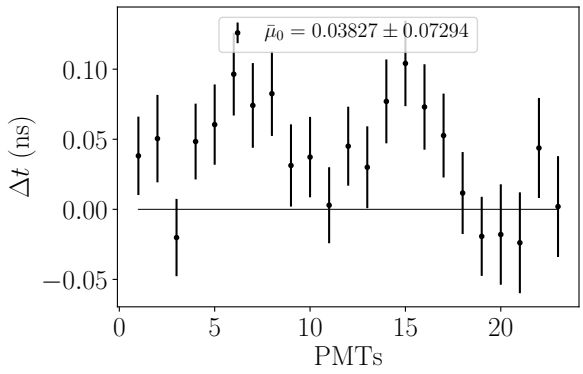

Figure 45: Relative time offsets from the global fit with σ_{combi} fixed and two additional Gaussians with fixed means for p-e combinations for all PMTs with TTS $\approx$ 1.7 ns.

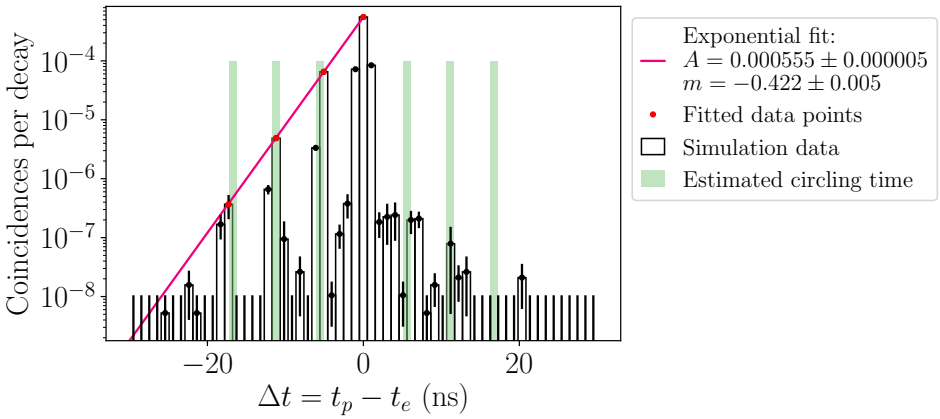

Figure 46: Δt-distribution for p-e combinations with PMTs without TTS at large time scales. The coincident rate is the sum of the rates of all p-e combinations normalized by the frequency of the type. The green areas are the roughly estimated circling times for a photon around the module in the glass. The red data points are fitted with an exponential function $f(x) = A\exp(-mx)$ shown in pink.

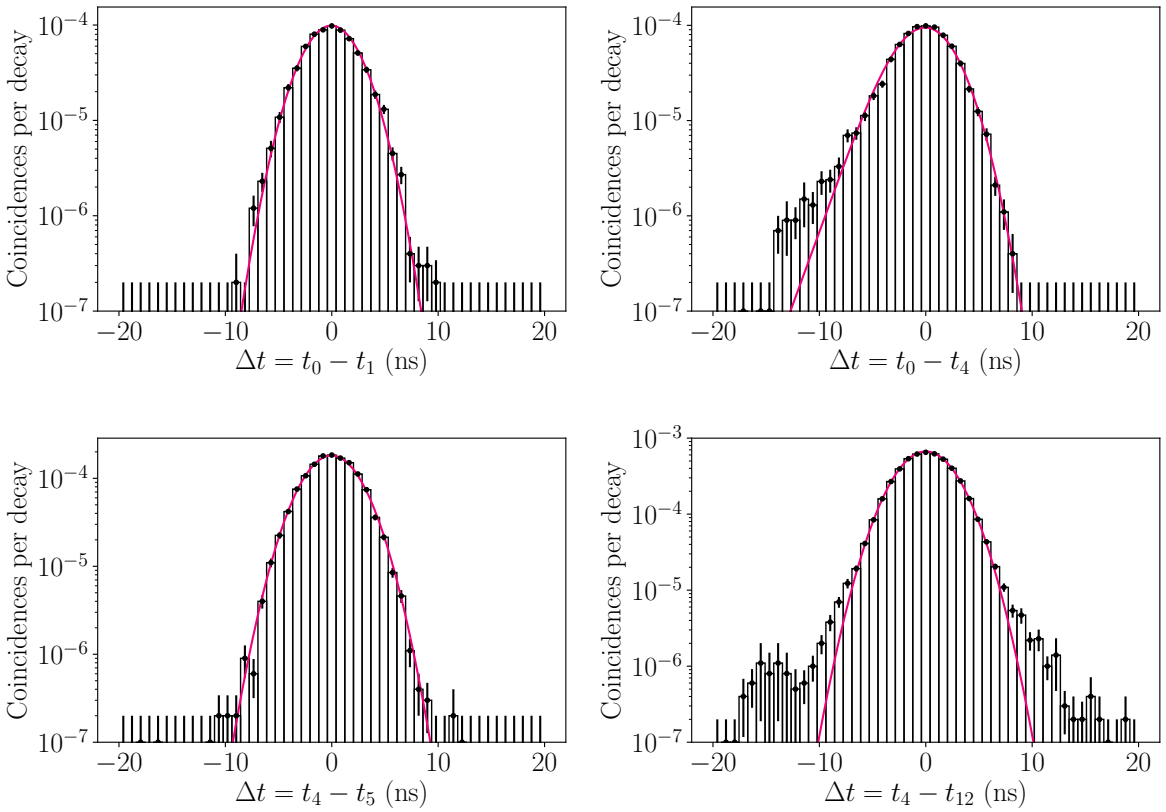

Figure 47: Δt-distribution and global fit with σ_{combi} fixedand convolution of Gaussian and exponential for p-e combinations for the PMT combinations exemplary for the types used for the calibration with TTS $\approx 1.7\,\text{ns}$.

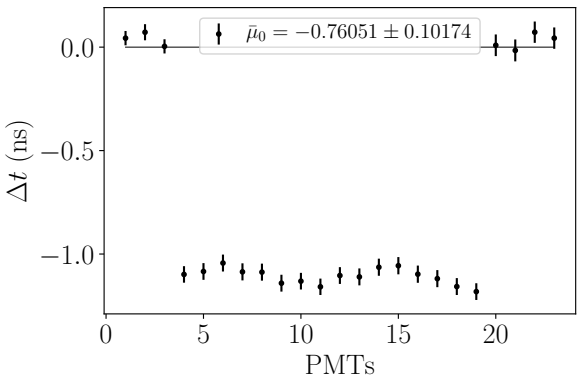

Figure 48: Relative time offsets from the global fit with σ_{combi} fixed and convolution of Gaussian and exponential for p-e combinations for all PMTs with TTS $\approx$ 1.7 ns.

6. Application of the Calibration Method to an Experimental Test Setup

The calibration method is not only studied with Geant4 simulations but also experimentally. For this purpose a setup is build with four PMTs in a half vessel (see Fig. 49), as an mDOM prototype is not yet available. Unfortunately complications inhibit the use of two PMTs, so only one PMT combination is left in the end for testing the calibration method. Before building the setup the radioactive contamination of the used glass vessel is investigated in detail (see Section 3.4). The PMT timing calibration of the experimental setup is done using Cherenkov light and with a reference measurement with an LED.

6.1. Experimental Setup

Figure 49: Experimental setup with four PMTs with reflectors and holding structure in a glass vessel to test the calibration method. Between the glass and the other components is a layer of gel. Left: without black tape from the front. Right: glass vessel in black tape from the back.

An experimental test of the calibration algorithm developed in this thesis was planned to be done with four PMTs in a half vessel, building one polar ring. The build setup can be seen in Fig. 49. The space between holding structure, reflectors, PMTs and glass is filled with silicone gel from QSI and the white holding structure printed by a 3D-printer is painted black at the outside with ordinary acrylic color (brand: Raphaëllo). The glass is covered with black tape to simulate optical properties of ice. Since the refractive index of air is about $n_{\text{air}} = 1$ and of the glass $n_{\text{glass}} = 1.48$, the total reflection angle at the

glass-air surface lies at about $\theta_{\text{crit}} = 42.51°$. For ice with an refractive index of $n_{\text{ice}} = 1.31$ the angle is $\theta_{\text{crit}} = 62.27°$, which means less reflection. In this experiment reflections are reduced due to absorptions from the black tape.

The serial numbers of the PMTs used are BA0373, BA0375, BA0534 and BA0535 (short 373,375,534,535) which are Hamamatsu R1299-01 HA MOD 3-inch PMTs. All of them have a so called HA coating to increase dark rate stability. The coating is conductive and is on the same potential level as the photocathode [4]. Since the dark rate decreases with the difference of reflector and photocathode potential [25], the reflectors were planed to be put on cathode potential. PMT 534 and 535 feature a conductive band leading from the cathode pin under the coating to the front of the PMT made by the manufacturer. The rest of the copper band emerging at the cathode is connect to the back of the reflectors, putting them on photocathode potential. Since PMT 373 and 375 lack a conductive band, a reflector connection is constructed from adhesive copper band. It is sticked on the back of the reflectors and over the outside of the PMTs to the cathode pin. Unfortunately the acrylic color on the holding structure is found to be electrically conductive, creating a connection between the reflectors and therefore between the photocathodes, which means the PMT signals could influence each other. The manually applied copper bands are hence removed from the cathode pins and PMT 535 is not used for the measurements. Building a new setup was not possible in the given time span. For the LED measurements, PMT 534 remains with the reflector on high voltage, which means all reflectors are on the same potential. At the time of the time calibration measurement using Cherenkov light, it was discovered that the reflectors at high voltage operate as receiver and amplifier for external noise, which was then observable with very high amplitudes in the PMT signals. Probably it was not noticeable at the LED measurement, because there the trigger was the LED signal, as explained in Section 6.2, and in the Cherenkov light measurement the trigger is one of the PMTs and therefore it was triggered on the high amplitude noise. The time calibration with Cherenkov light was therefore done with the two PMTs whose cathode-reflector connection could be used, namely PMT 373 and 375. The LED calibration is discussed for these two PMTs only as well.

6.2. Reference Calibration via LED

In order to compare the calibration method investigated in this thesis, the time calibration is also done with an LED. The setup build for this purpose is shown in Fig. 50. The LED is placed at the inside of the half vessel with the four PMTs, since the outside of the glass vessel is covered with back tape. Therefore the photons are not directly emitted onto the photocathode, but have to travel through the PMTs from back to front. Because of this complicated light path, the intensity of the LED has to be quite high. A diffuser is placed in front of it to get a more isotropic light source. Due to the extensions of the diffuser and the LED, they could not be placed directly at the glass window at the and of the PMTs, but had to be placed above the bases and cables. PMT 535 is completely covered with isolating tape and so is the base of PMT 375 to prohibit any interaction

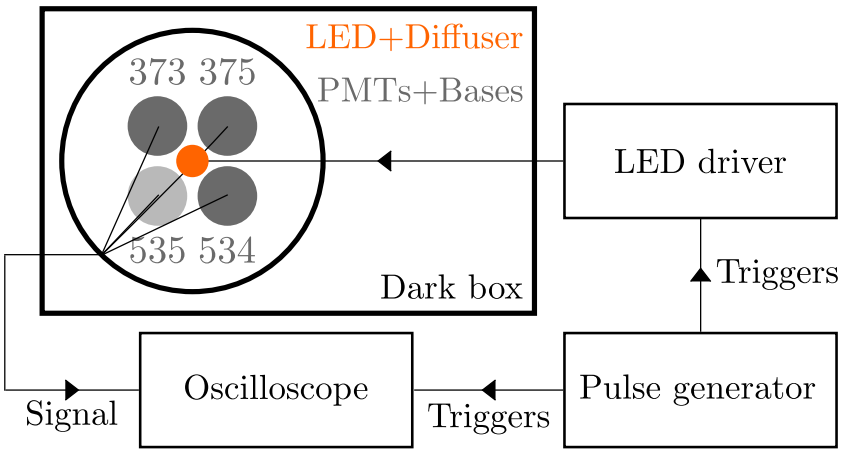

Figure 50: Schematic experimental setup for the time calibration with an LED. PMT 535 in lighter gray is not used in the measurement.

between the bases.

The LED is triggered by a pulse generator, which also triggers the oscilloscope[3] to record the signal from the PMTs. The collected data are processed and analysed at the computer. The trigger signal has a width of 16 ns and is sent every 100 μs. The trigger for the picoscope is on the leading edge at 50 mV. After the trigger the PMT signals are recorded for 120 ns, which is called a waveform. The time of the minimum of the waveform for each PMT signal is saved if it is smaller than -4 mV. In addition the amplitude and charge of the corresponding pulse is saved, where the integral boundaries for the charge calculation are the points where the signal overshoots the baseline at -2 mV first on either side of the maximum. A histogram of the recorded times gives the transit time distribution of the PMTs with the TTS influencing its standard deviation. Another influence on the width of the time distribution are possibly varying paths of the photons by reflections. The time difference between the PMTs can be calculated from the differences of the mean of the distributions:

$$\Delta t_{i,j} = \mu_i - \mu_j. \tag{26}$$

Here $\Delta t_{i,j}$ is the time difference between PMTs i and j and μ_i the mean of the transit time distribution of PMT i. The uncertainty for Δt is given by the statistical uncertainty calculated by Gaussian error propagation plus a systematic uncertainty due to the position of the LED. In eq. (26) it is assumed that the distance from the light source to the photocathode is the same for every PMT. This is not the case, since the positioning of the LED is done manually and the setup is not symmetric for all PMTs. Therefore an uncertainty in distance of 3 cm is assumed. The uncertainty for Δt is then given by

$$u(\Delta t_{i,j}) = \sqrt{(u(\mu_i))^2 + (u(\mu_j))^2} + \frac{3\,\mathrm{cm}}{c} \tag{27}$$

[3]PicoScope® 6000 Series Oscilloscopes with four channels.

where $u(\mu_i)$ is the uncertainty of μ_i and c the speed of light in vacuum.

For the time distributions shown in Fig. 51 10^5 waveforms were measured. The dis-

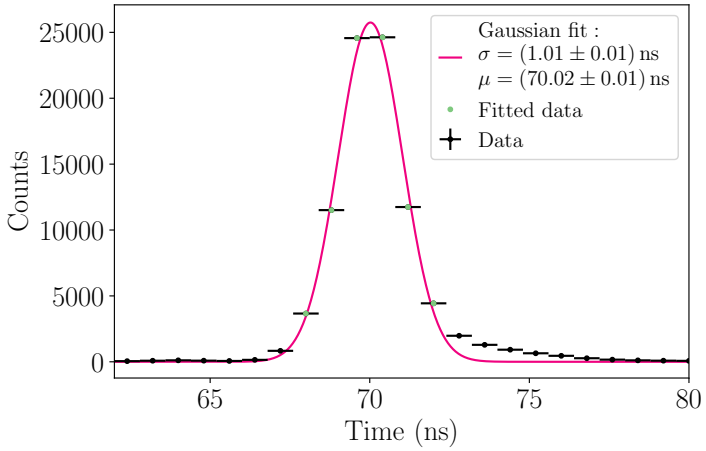

(a) PMT 373

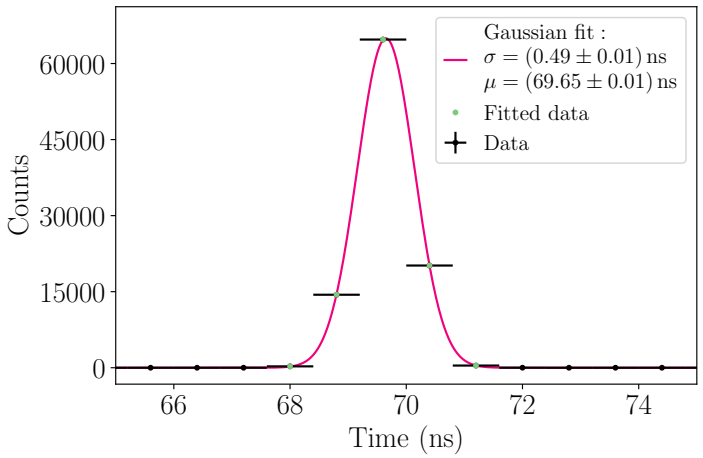

(b) PMT 375

Figure 51: Time distribution of the waveform minima for the different PMTs. The horizontal bars give the size of the bins. The statistical uncertainties on the counts are represented by vertical bars but are smaller than the point size. For the Gaussian fits only the marked data points are used.

tributions were fitted with a Gaussian with variable amplitude. The means are at $\mu_{373} = 70.02 \pm 0.01\,\text{ns}$ and $\mu_{375} = 69.65 \pm 0.01\,\text{ns}$ with a resulting time differences of $\Delta t_{373,375} = t_{373} - t_{375} = (0.37 \pm 0.15)\,\text{ns}$. Two significant differences between the time distributions is their amplitude and standard deviation, where large amplitude goes with small σ and vice versa. PMT 375 has less than half of the amplitude of PMT 373. The standard deviations are at $\sigma_{373} = (1.01 \pm 0.01)\,\text{ns}$ and $\sigma_{375} = (0.49 \pm 0.01)\,\text{ns}$. To

investigate these differences, the mean photoelectron numbers μ(pe) per pulse are calculated laying at $\sim$13.0 for PMT 373 and $\sim$2.6 for PMT 375. An increase in μ(pe) comes with a decrease in measured TTS and a larger number of photons hitting a PMT leads to a larger μ(pe). This is in agreement with the observations made on amplitude and standard deviation of the fitted Gaussians. The decreased number of detected photons for PMT 375 could be influenced by the tape wrapped around the base, since it prevents light incident on the glass window from some angles.

The origin of the time difference between the two PMTs is probably a different transit time. The signal cables are of the same length, so there is no offset introduced by different cable length. Another possible contribution to the time difference could be generated by the asymmetric experimental setup. As already mentioned the base of PMT 375 is covered with black tape, so that this PMT has effectively a smaller field of view. Other asymmetries are given by the taped PMT 535 and the cables going out of the module above PMT 535. The uncertainty on the placement of the LED is already taken into account, but not the uncertainty on the orientation. The measured time difference between the PMTs corresponds to a distance in air of about 10 cm covered by a photon. It was not investigated what impact a differently oriented LED would have.

6.3. Calibration using Background from Vessel Glass

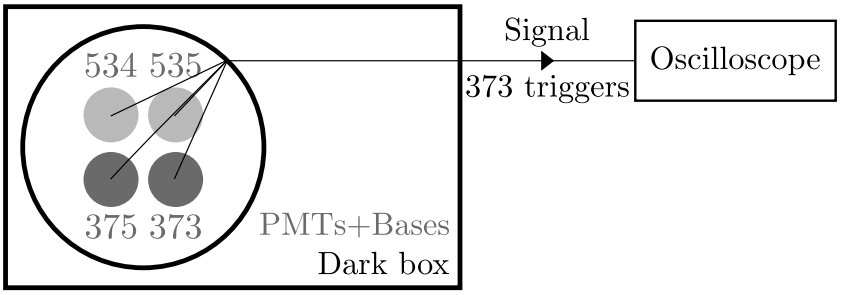

Figure 52: Schematic experimental setup for the time calibration using background light from the glass vessel. PMT 534 and 535 in lighter gray are not used in the measurement.

The experimental setup for the time calibration using Cherenkov light can be seen in Fig. 52. The setup uses the same readout as the LED measurement. Another difference is the trigger for the oscilloscope, which is now the PMT 373 at 20 mV on the rising edge. The measured waveforms reach from 24 ns before the trigger to 56 ns after the trigger. One pulse of each waveform from PMT 375 is registered if its amplitude is larger than 20 mV. As before the time and amplitude of the maximum as well as the charge of the pulse are saved. The trigger was set at a higher level because Cherenkov decays lead to the emission of many photons, depending on the energy of the charged particle, in a short period of time.

The resulting time difference distribution can be seen in Fig. 53. For the Gaussian fit only selected data points where taken, because of the sudden broadening of the peak at a view nanoseconds at each side of the peak. To find out about the origin of this broadening, the hit times of the PMTs were investigated (see Fig. 54). There are no hit times of PMT 373 before 24 ns since the triggered was on the rising edge. The hit time distribution of PMT 375 tends also towards larger hit times, maybe because the probability of PMT 373 to be triggered is highest for decays happening close to it, and therefore the photons need time to travel to PMT 375. In the hit time distribution of PMT 373 there is a small peak at about 28 ns to 29 ns. This led to the idea to cut on different hit times of PMT 373 and look at the time difference distribution again. Taking only hit times larger than 28 ns leads to a Δt-distribution with two peaks, one at -4 ns and one at about 0 ns (left in Fig. 55). When increasing the cutoff further to 30 ns there is only one peak left at about -5 ns (right in Fig. 55). Cutting on the hit times of PMT 375 shows the same phenomenon, although with a much smaller peak at about 5 ns (see Fig. 56). These peaks at roughly ± 5 ns indicate that the broadening of the peak of the Δt-distribution without cuts is not caused by a continuous process, but by a process which has an impact only at a specific time. Such a process would be photons somehow traveling around in the glass vessel and hitting one of the PMTs after one "circuit" as already seen in the simulation studies. Although "circuit" might

not be the right word here, since there is only one half-vessel in the experimental setup, but the light path might be one that gets somehow reflected at the end of the half-vessel.

The relative time difference between the two PMTs from the Cherenkov measurement of (0.04 ± 0.05) ns, where the uncertainty is given by the fit uncertainty, is in good agreement with the time offset of (0.37 ± 0.15) ns calculated from the LED measurement. The calibration method using Cherenkov light from radioactive decays therefore seem to work with this simple setup of two PMTs.

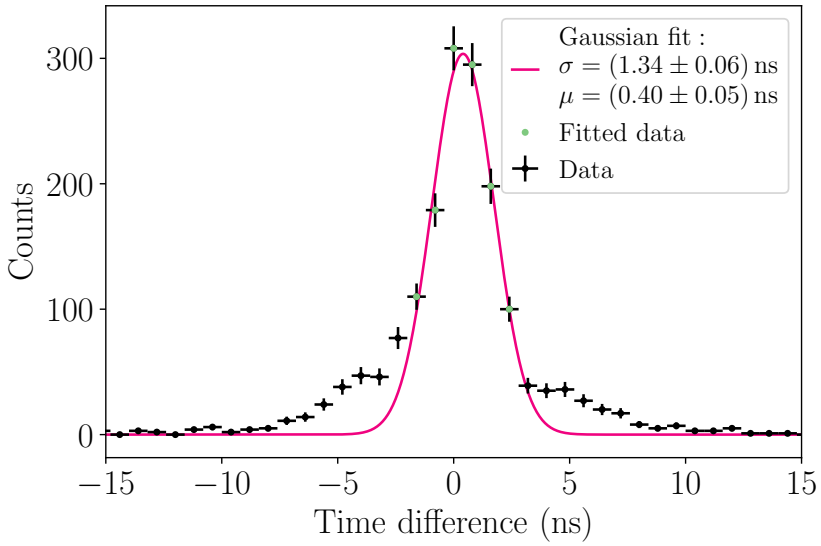

Figure 53: Δt-distribution for PMTs 373 and 375 with $\Delta t = t_{373} - t_{375}$. The horizontal bars represent the size of the bins, the vertical bars the statistical uncertainties on the counts. For the Gaussian fit only the marked data points are used. Uncertainties on μ and σ are the fit uncertainties.

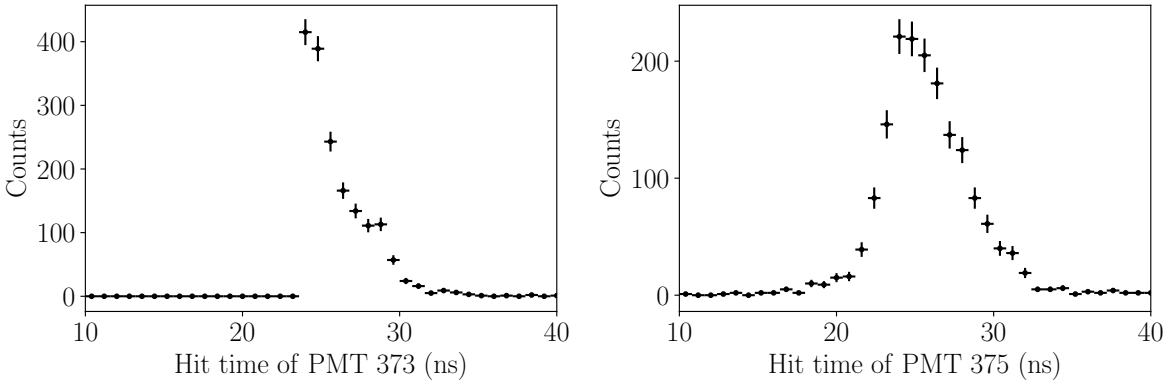

Figure 54: Hit times for PMTs 373 and 375. The horizontal bars represent the size of the bins, the vertical bars the statistical uncertainties on the counts.

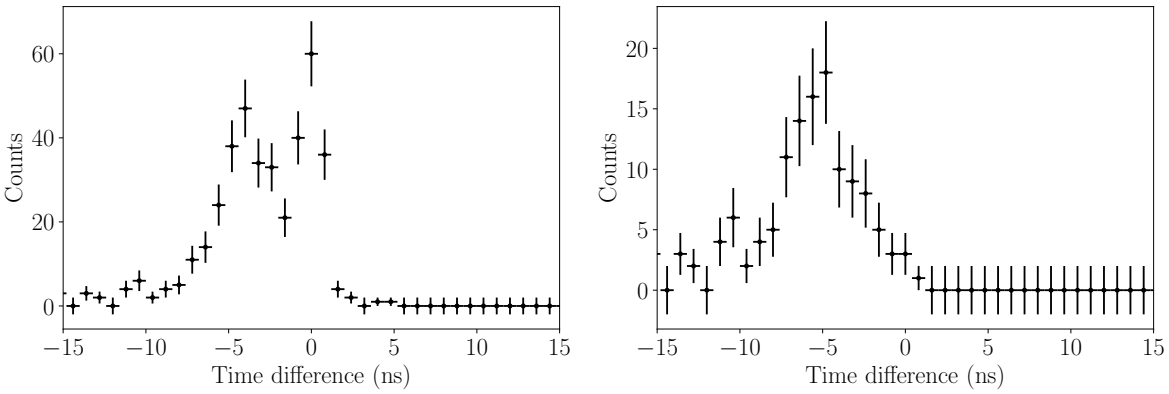

Figure 55: Δt-distribution for PMTs 373 and 375 with $\Delta t = t_{373} - t_{375}$ with $t_{373} \geqslant 28\,\mathrm{ns}$ (left) and $t_{373} \geqslant 30\,\mathrm{ns}$ (right). The horizontal bars represent the size of the bins, the vertical bars the statistical uncertainties on the counts.

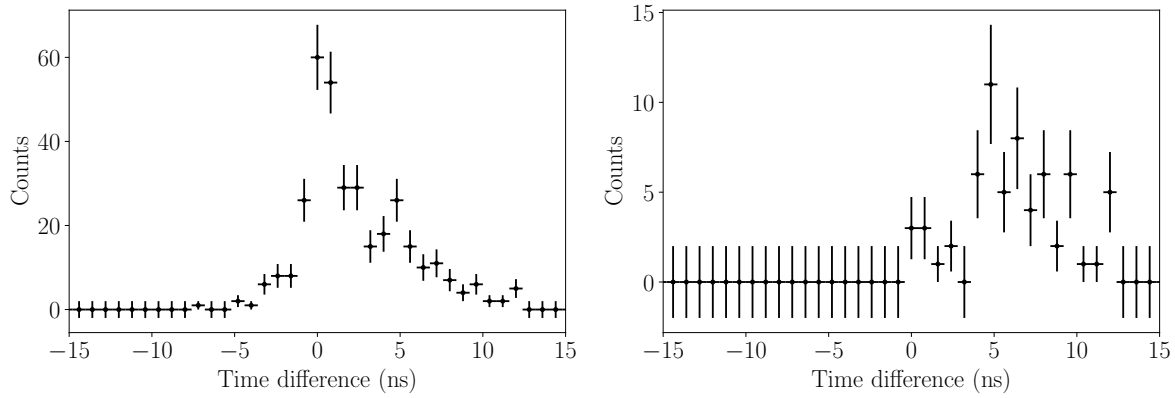

Figure 56: Δt-distribution for PMTs 373 and 375 with $\Delta t = t_{373} - t_{375}$ only containing time differences with $t_{375} \geqslant 28\,\text{ns}$ (left) and $t_{375} \geqslant 30\,\text{ns}$ (right). The horizontal bars represent the size of the bins, the vertical bars the statistical uncertainties on the counts.

7. Summary and Outlook

The time and efficiency calibration of the optical modules used in a Cherenkov neutrino detector is of importance for the reconstruction accuracy of neutrino energy and direction. In this thesis a calibration method for a new optical module including multiple PMTs for an upgrade of the IceCube Neutrino Observatory, the mDOM, was investigated. The method uses Cherenkov light from radioactive decays in the vessel glass of the mDOM and should be used to calibrate the PMTs in one module. The time calibration with this method was tested with a Geant4 simulation and an experimental test setup.

The calibration method was used for the calibration of a similar optical module in KM3NeT [23]. It uses the time difference distribution of twofold coincidences between two PMTs, which is given by a Gaussian with the mean equal to the time offset between those two PMTs. It had to be investigated whether the calibration method had to be and could be adapted for the mDOM due to two major differences. First the calibration in KM3NeT makes use of ^{40}K decays in the sea water surrounding the module and second is the KM3NeT optical module spherical in shape.

Gamma spectroscopy of a Vitrovex glass vessel showed that ^{40}K is the isotope with dominating activity, although a measurement of a glass vessel from a different production batch showed no measurable amount of ^{40}K [19] indicating that the ^{40}K concentration is strongly depending on the production batch. Nevertheless the simulation studies were done using only ^{40}K decays. ^{40}K can produce Cherenkov light in most cases through the electron emitted at the β^- decay with a maximal energy of about 1.3 MeV overcoming the Cherenkov threshold in glass of about 0.18 MeV. Since several other isotopes of the natural decay chains also occurring in the glass produce electrons and positrons that can overcome this threshold too, further simulation studies could be done including these isotopes. The difference is the different energy and therefore a different amount of produced photons and a different Cherenkov angle.

The simulation studies included hit and coincidence rates of the PMTs in the mDOM and investigations of the time difference distributions for PMTs with perfect and realistic time distribution (TTS = 0 ns and TTS $\neq$ ns). The PMTs of the mDOM can be divided in two categories, the equatorial PMTs partly lying in the cylindrical part of the module, and the polar PMTs at the spherical poles of the mDOM. Equatorial PMTs have a higher hit rate than polar ones due to the asymmetry of the module. This causes also different coincidence rates of geometrically different PMT combinations. The time difference distributions (Δt-distributions) of different PMT combinations are also differently shaped. The shape of the Δt-distributions and the coincidence rate led to the choice of using four geometrically different PMT combinations for the calibration.

In order to enable the calibration of the whole module, an asymmetric time difference distribution between a polar and an equatorial PMT had to be included into the calibration. The calibration in the simulation was done using an global fit, where the fit

functions of all used PMT combinations are fitted at once. When using a simple Gaussian fit a relative time offset of the equatorial PMTs occurs, greatly depending on the TTS of the PMTs. The largest offset was found for the largest TTS. For TTS=0.5 ns there was no significant offset, but most PMTs had negative time offsets. For TTS=1 ns and TTS$\approx$ 1.7 ns the equatorial PMTs had significant positive time offsets of at most 0.10 ns and 0.37 ns respectively. The time offsets could be reduced to below 0.08 ns for TTS=1 ns and 0.14 ns for TTS$\approx$ 1.7 ns by the fit of one additional Gaussians to the first side maximum seen at small TTS for the PMT combination of an equatorial and polar PMT (p-e). Another ansatz fitting those p-e distributions with the convolution of a Gaussian with an exponential led to an increase of the magnitude of the offset for equatorial PMTs. If no suitable fit function for the asymmetric time difference distribution is found, simulation studies could be used to determine the intrinsic offsets of the PMTs. Since the origin of these offsets are the geometry and material properties of the mDOM and thus they should be able to be determined by a proper simulation at fixed TTSs. Possibly a likelihood-function could be used for the calibration using the results of such stimulation studies. Simulation studies should also be done on the variability of the offsets depending on fluctuations in geometry and material properties caused by the production process.

An experimental test of the calibration algorithm was not possible and also not experimental test of one polar and one equatorial PMT. But it was shown on two polar PMTS that in principle the calibration method is applicable to the mDOM. The experimental test of the calibration method with two PMT successfully determined time offset between them is in good agreement with a reference calibration using an LED. The uncertainty of the calibration using Cherenkov light is here 0.06 ns on a time difference of 0.37 ns.

The investigated calibration method seems to execute the time calibration of the PMTs in one mDOM with sufficient accuracy. The studies of this thesis show that a hardware-independent in-situ calibration method for PMT timing is possible for the mDOM. Further investigations on the efficiency calibration have to be done.

A. Hit Time Difference Distributions with Perfect Time Resolution

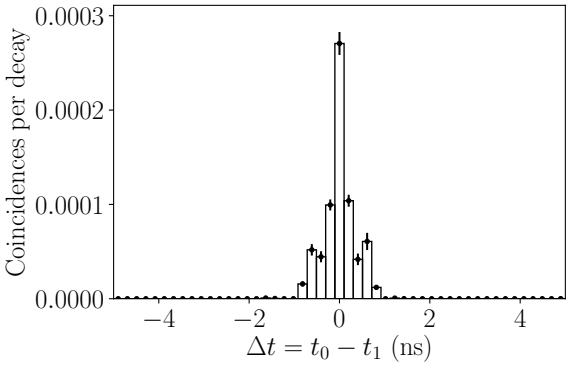

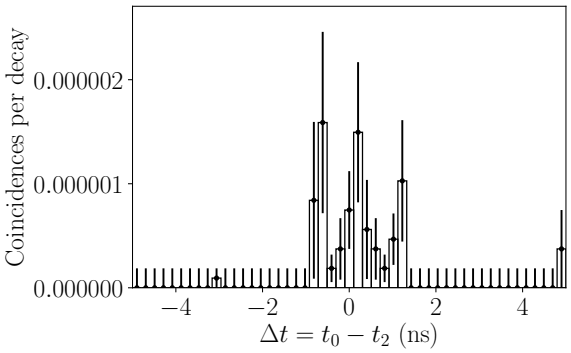

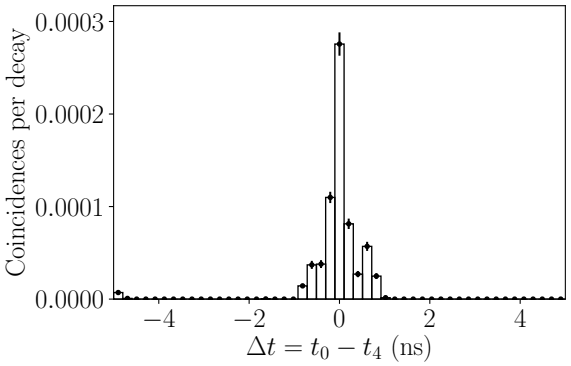

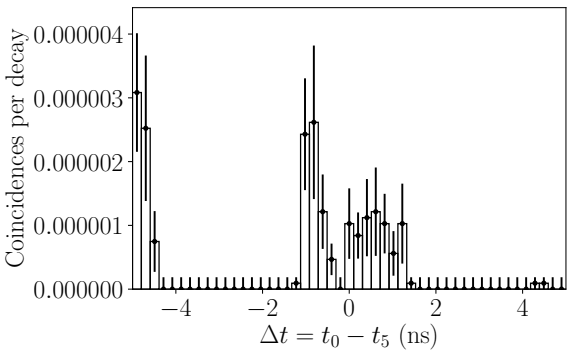

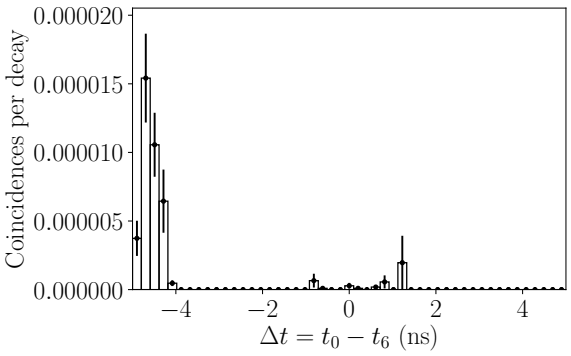

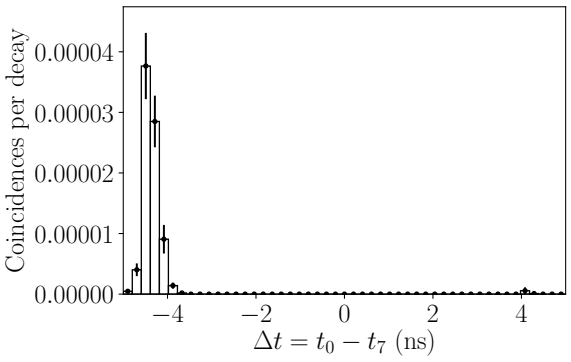

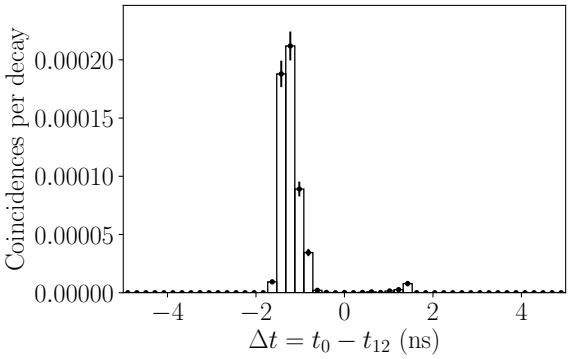
Coincidences per decay
0.00020
0.00015
0.00010
0.00005
0.00000
−4
−2
0
2
4
$\Delta t = t_0 - t_{12}$ (ns)

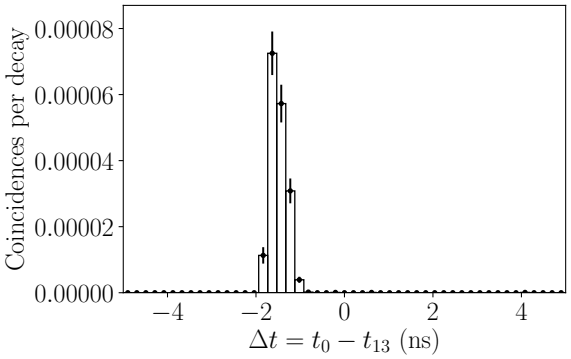
Coincidences per decay
0.00008
0.00006
0.00004
0.00002
0.00000
−4
−2
0
2
4
$\Delta t = t_0 - t_{13}$ (ns)

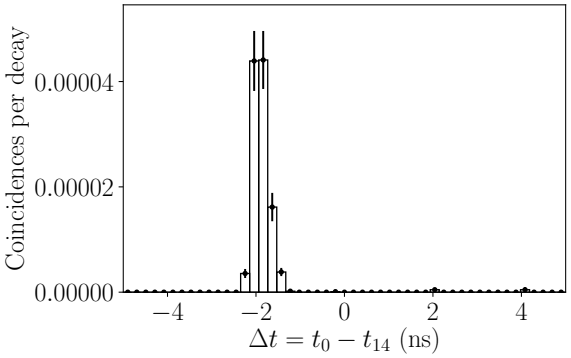
Coincidences per decay
0.00004
0.00002
0.00000
−4
−2
0
2
4
$\Delta t = t_0 - t_{14}$ (ns)

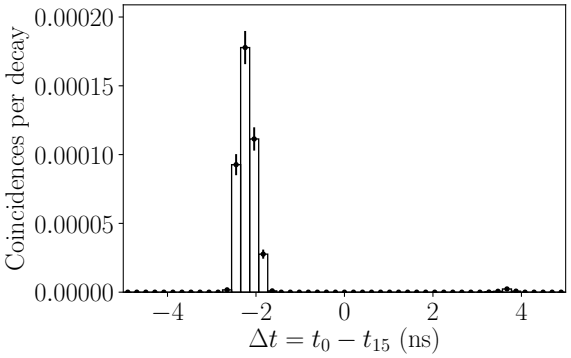
Coincidences per decay
0.00020
0.00015
0.00010
0.00005
0.00000
−4
−2
0
2
4
$\Delta t = t_0 - t_{15}$ (ns)

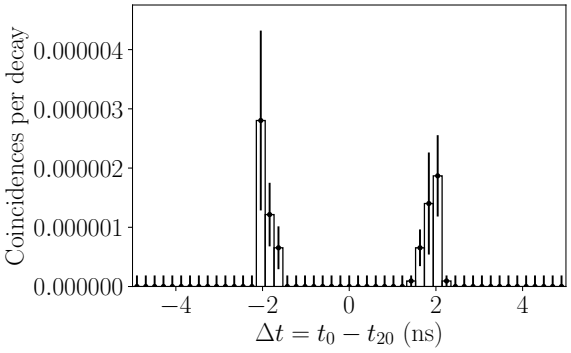
Coincidences per decay
0.000004
0.000003
0.000002
0.000001
0.000000
−4
−2
0
2
4
$\Delta t = t_0 - t_{20}$ (ns)

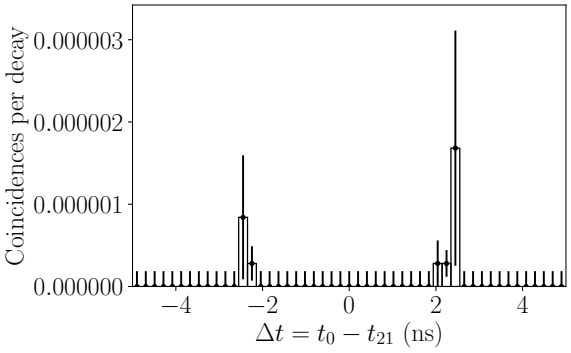
Coincidences per decay
0.000003
0.000002
0.000001
0.000000
−4
−2
0
2
4
$\Delta t = t_0 - t_{21}$ (ns)

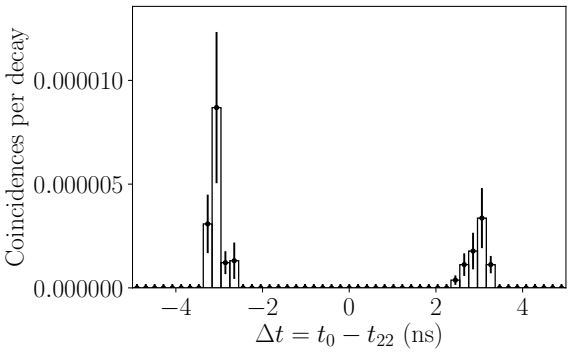
Coincidences per decay
0.000010
0.000005
0.000000
−4
−2
0
2
4
$\Delta t = t_0 - t_{22}$ (ns)

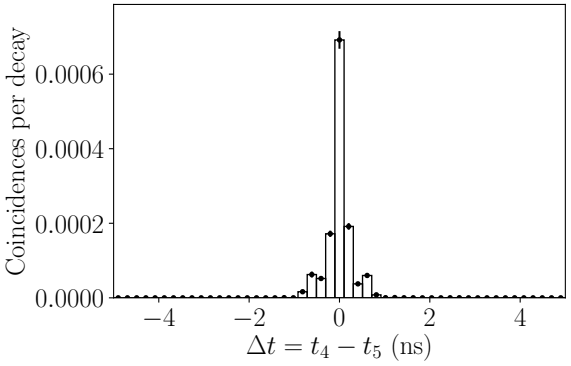
Coincidences per decay
0.0006
0.0004
0.0002
0.0000
−4
−2
0
2
4
$\Delta t = t_4 - t_5$ (ns)

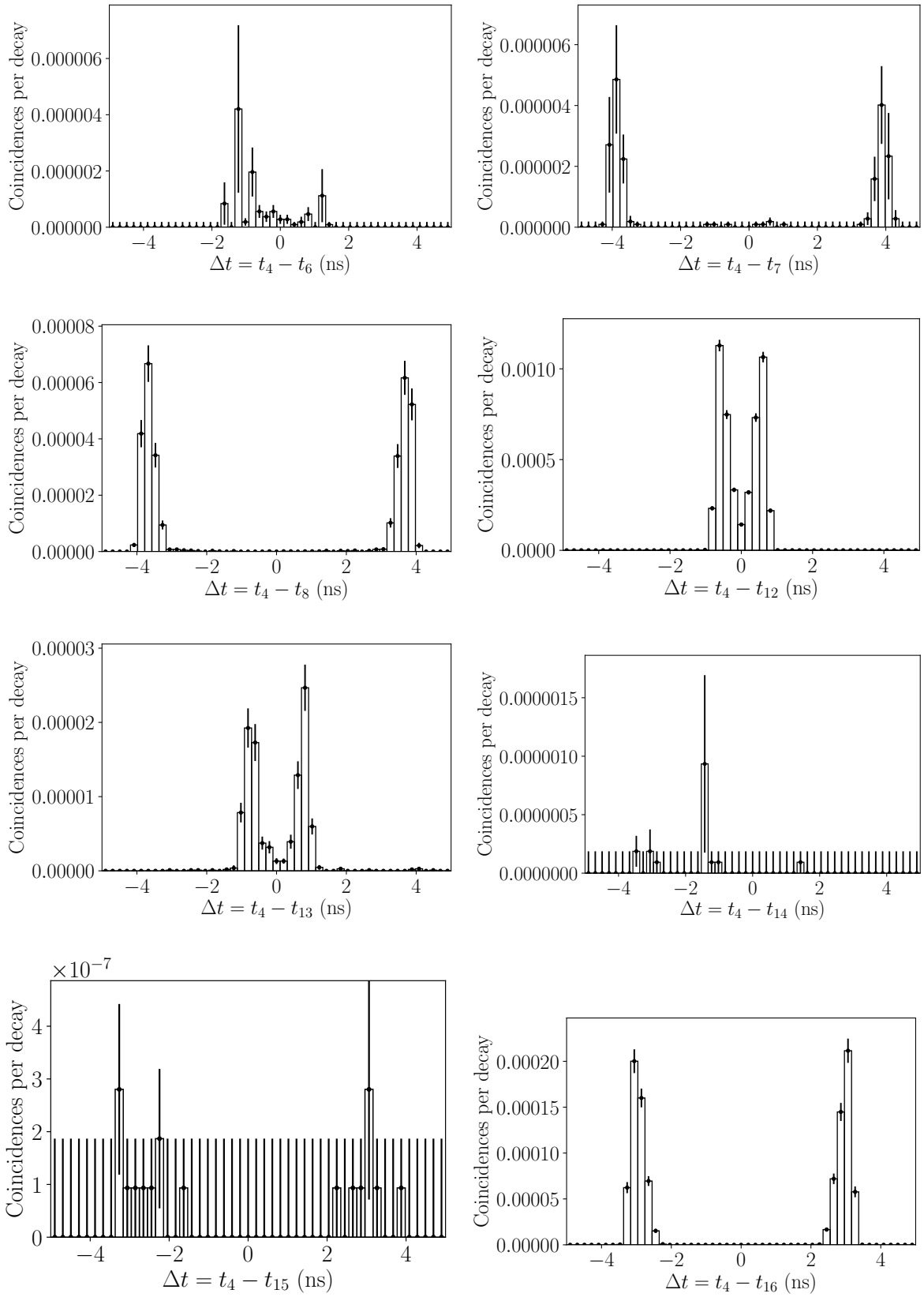

Figure 56: This page and two previous pages: Δt-distributions for exemplary PMT combinations, one for each geometrically different PMT combination of the mDOM. PMTs with perfect time resolution (TTS=0).

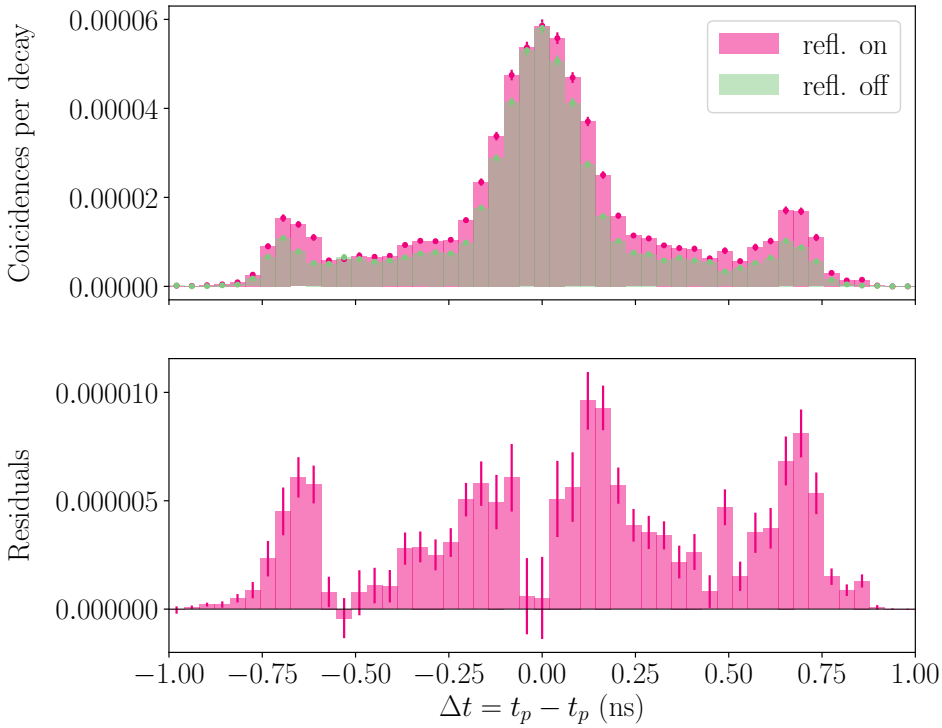
Coicidences per decay
0.00006
0.00004
0.00002
0.00000
refl. on
refl. off
Residuals
0.000010
0.000005
0.000000
−1.00
−0.75
−0.50
−0.25
0.00
0.25
0.50
0.75
1.00
$\Delta t = t_p - t_p$ (ns)

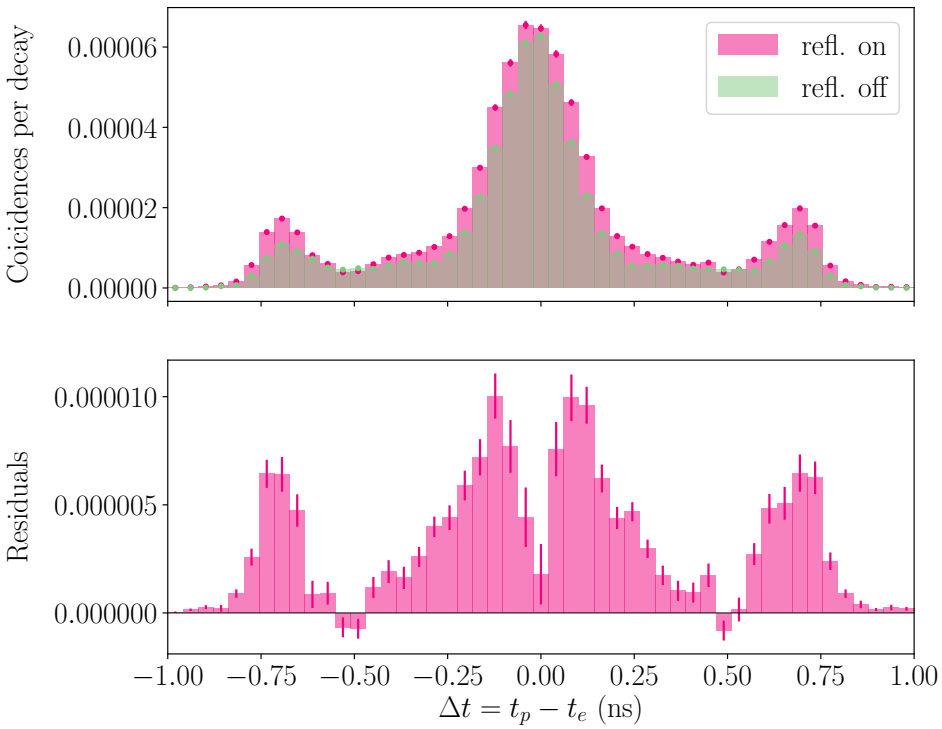
Coicidences per decay
0.00006
0.00004
0.00002
0.00000
refl. on
refl. off
Residuals
0.000010
0.000005
0.000000
−1.00
−0.75
−0.50
−0.25
0.00
0.25
0.50
0.75
1.00
$\Delta t = t_p - t_e$ (ns)

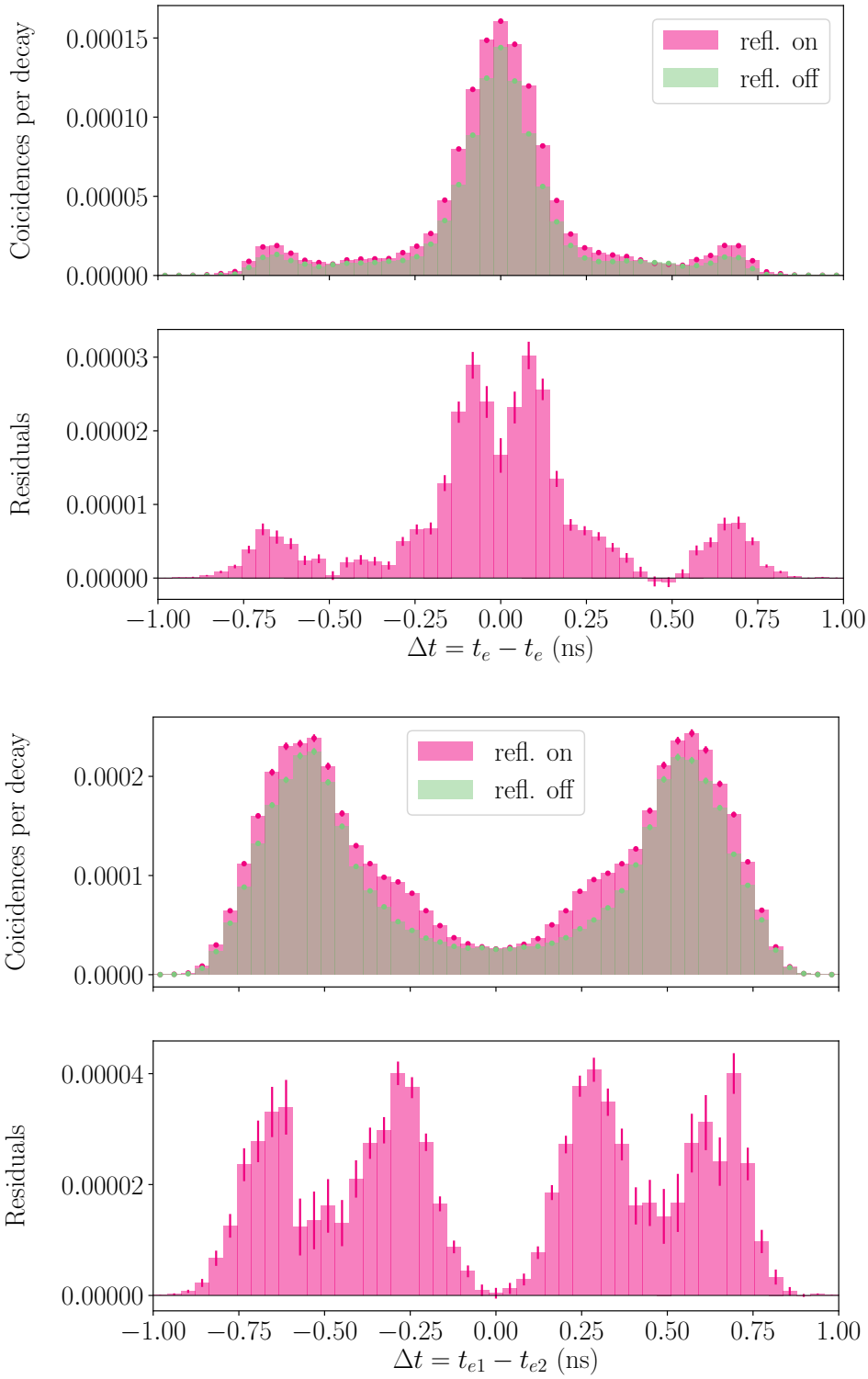

Figure 56: This and previous page: Δt-distributions with reflecting (refl. on) and absorbing cones (refl. off) for the PMT combination types used for the calibration with PMTs without TTS=0.

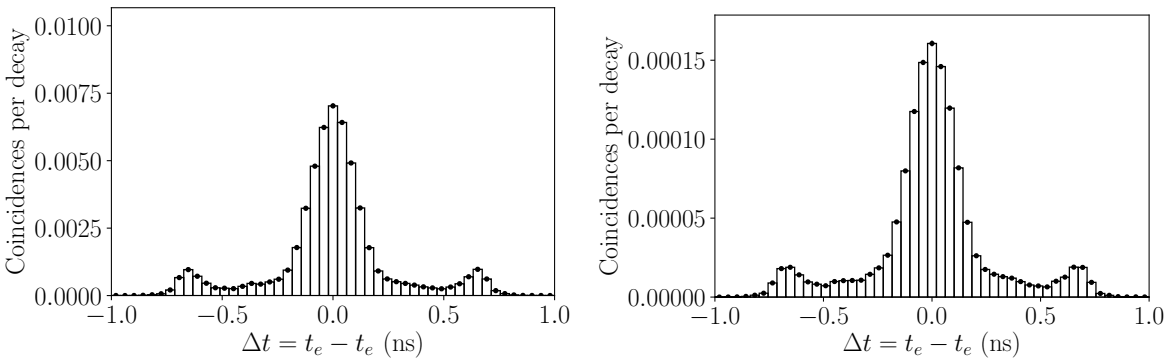

Figure 57: Comparison of an exemplary Δt-distribution between the simualtion used in this thesis (right) including the killing of photons 100 ns after the decay and a simulation without this cutoff (left), but with another gel and without QE.

Literatur

[1] M. G. Aartsen et al. The IceCube Neutrino Observatory: Instrumentation and Online Systems. *JINST*, 12(03):P03012, 2017.

[2] M. G. Aartsen et al. IceCube-Gen2: A Vision for the Future of Neutrino Astronomy in Antarctica. 2014.

[3] Icecube gen2 and icecube upgrade. `https://meetings.triumf.ca/indico/event/27/session/5/contribution/26/material/slides/0.pdf.`, November 3rd 2018.

[4] Lew Classen. *The mDOM - a multi-PMT digital optical module for the IceCube-Gen2 neutrino telescope.* PhD thesis, Friedrich-Alexander-Universität Erlangen-Nürnberg, February 2017.

[5] Markus Ahlers and Francis Halzen. Opening a New Window onto the Universe with IceCube. *Prog. Part. Nucl. Phys.*, 102:73–88, 2018.

[6] Björn Herold. *Hardware studies, in-situ prototype calibration and data analysis of the novel multi-PMT digital optical module for the KM3NeT neutrino telescope.* PhD thesis, Friedrich-Alexander-Universität Erlangen-Nürnberg, 2017.

[7] Annarita Margiotta. The KM3NeT deep-sea neutrino telescope. *Nucl. Instrum. Meth.*, A766:83–87, 2014.

[8] M. Tanabashi et al. Review of particle physics. *Phys. Rev. D*, 98:030001, Aug 2018.

[9] Thomas K. Gaisser, Ralph Engel, and Elisa Resconi. *Cosmic Rays and Particle Physics.* Cambridge University Press, 2 edition, 2016.

[10] Ch. Spiering U.F. Katz. High-energy neutrino astrophysics: Status and perspectives. *Progress in Particle and Nuclear Physics*, 67(651-704), 2012.

[11] Matthew G. Baring. Diffusive shock acceleration: The Fermi mechanism. In *Very high-energy phenomena in the universe. Proceedings, 32nd Rencontres de Moriond, Les Arcs, France, January 18-25, 1997*, pages 97–106, 1997.

[12] J. A. Formaggio and G. P. Zeller. From ev to eev: Neutrino cross sections across energy scales. *Rev. Mod. Phys.*, 84:1307–1341, Sep 2012.

[13] PAVEL ALEKSEJEVIČ ČERENKOV, IL'JA MICHAJLOVIČ FRANK, IGOR' EVGEN, and EVIČ TAMM. Physics 1958. In *Physics 1942-1962*, pages 421 – 483. Elsevier, 2013.

[14] I. M. Frank and I. E. Tamm. Coherent visible radiation of fast electrons passing through matter. *Compt. Rend. Acad. Sci. URSS*, 14(3):109–114, 1937. [Usp. Fiz. Nauk93,no.2,388(1967)].

[15] Thorsten Gluesenkamp. *On the Detection of Subrelativistic Magnetic Monopoles with the IceCube Neutrino Observatory.* PhD thesis, Rheinisch-Westfälische Technische Hochschule Aachen, October 2010.

[16] D F Cowen and the IceCube Collaboration. Tau neutrinos in icecube. *Journal of Physics: Conference Series*, 60(1):227, 2007.

[17] Hamamatsu Photonics K.K. Photomultiplier tubes - basics and applications. `https://www.hamamatsu.com/resources/pdf/etd/PMT_handbook_v3aE.pdf`, 2007. Third edition. Accessed 18.12.2018.

[18] A.G. Wright. *The Photomultiplier Handbook.* Oxford University Press, 1 edition, 2017.

[19] Martin Antonio Unland Elorrieta. Studies on dark rates induced by radioactive decays of the multi-pmt digital optical module for future icecube extensions. Master's thesis, Westfälische Wilhelms-Universität Münster and Universidad de Sevilla, December 2017.

[20] C. Marmonier S.-O. Flyckt. *PHOTOMULTIPLIER TUBES - principles & applications.* Photonics, September 2002.

[21] Board of Regents of the University of Wisconsin System University of Wisconsin-Madison Physical Sciences Lab. Digital optical modules. `http://www.psl.wisc.edu/projects/large/icecube/more-icecube/dom`, 2018.

[22] L. Classen. private communication.

[23] Jonas Reubelt. *Simulation and measurement of optical background in the deep sea using a multi-PMT optical module.* PhD thesis, Friedrich-Alexander-Universität Erlangen-Nürnberg, 2018.

[24] Daan van Eijk Chris Wendt Ken Clark Summer Blot Josh Hignight John Kelly Claudio Kopper Jason Koskinen, Timo Karg. Om requirements task force - status report, August 15th 2018.

[25] M. Unland et al. Characterization of the hamamatsu r12199-01 ha for low temperature applications.

[26] KM3NeT. `https://www.km3net.org/news-media/album-optical-module/`, Accessed 03.01.2019.

[27] International Atomic Energy Agency (IAEA) Nuclear Data Section. Live chart of nuclides. `https://www-nds.iaea.org/relnsd/vcharthtml/VChartHTML.html`, 2018. Accessed 18.12.2018.

[28] S. Agostinelli et al. Geant4-a simulation toolkit. *Nuclear Instruments and Methods in Physics Research Section A: Accelerators, Spectrometers, Detectors and Associated Equipment*, 506(3):250 – 303, 2003.

[29] Gordon R. Gilmore. *Practical Gamma-Ray Spectrometry.* John Wiley & Sons, Ltd, second edition, 2008.

[30] MIRION Technologies. `http://www.canberra.com/literature/fundamental-principles/pdf/Gamma-Xray-Detection.pdf`.

[31] MIRION Technologies. `http://www.canberra.com/literature/fundamental-principles/pdf/Spectrum-Analysis.pdf`.

[32] R.E.F̃aw J.K.S̃hultis. *Fundamentals of Nuclear Science and Engineering.* CRC Press, third edition, 2016.

[33] Geant4 Collaboration. Geant4 user's guide for application developers. `http://geant4-userdoc.web.cern.ch/geant4-userdoc/UsersGuides/ForApplicationDeveloper/html/index.html`, 4. December 2015.

[34] Cristian Jesus Lozano Mariscal. Studies on the sensitivity of multi-pmt optical modules to supernova neutrinos in the south pole ice. Master's thesis, Westfälische Wilhelms-Universität Münster and Universidad de Sevilla, January 2017.

Danksagung